minerals

MDPI

Article

Geochemistry and U-Pb-Hf Geochronology of Mesoarchean Granitoids from the Arco Verde Complex: Implications for the Crustal Evolution of the Rio Maria Domain, Carajás Province

Bruna Karine Correa Nogueira [1,*], Jean-Michel Lafon [1,2], João Marinho Milhomem Neto [1,2], Fábio dos Santos Pereira [2], Regina Celia dos Santos Silva [3] and Elton Luiz Dantas [4]

1 Programa de Pós-Graduação em Geologia e Geoquímica, Instituto de Geociências, Universidade Federal do Pará, Belém CEP 66075-110, PA, Brazil; lafonjm@ufpa.br (J.-M.L.); milhomem@ufpa.br (J.M.M.N.)
2 Laboratório de Geologia Isotópica, Instituto de Geociências, Universidade Federal do Pará, Belém CEP 66075-110, PA, Brazil; fabiopereira@ufpa.br
3 SGB—Serviço Geológico do Brasil, Avenida Dr. Freitas, 3645, Belém CEP 66095-110, PA, Brazil; regina.santos@sgb.gov.br
4 Instituto de Geociências, Universidade de Brasília (UnB), St. Campus Universitário Darcy Ribeiro—Gleba A, Asa Norte, Brasília CEP 70910-900, GO, Brazil; elton@unb.br
* Correspondence: brunanogueira2611@gmail.com

Abstract

The Arco Verde Complex, exposed in the Serra do Inajá region of the Rio Maria Domain (Carajás Province, Amazonian Craton), represents one of the oldest TTG granitoid association of the province (3.00–2.92 Ga). While TTG magmatism is well constrained in the northern domain, its southern sector lacks precise geochronological data. This study integrates petrographic, geochemical, U–Pb zircon geochronology, and Nd–Hf isotopes to constrain the age, source, and crustal significance of these granitoids. Uranium–Pb zircon dating of two granodiorites yielded ages of 2979 ± 8 and 2979 ± 11 Ma, extending the 2.98 Ga TTG magmatic episode to the southern sector of the Rio Maria Domain. Geochemical data indicate dominant tonalites formed by partial melting of a similar mafic source at different crustal depths, whereas subordinate granodioritic and monzogranitic rocks show transitional TTG affinities. These features indicate coeval mafic and felsic crust rapidly reworked after formation. Hf and Nd model ages of 3.0–3.2 Ga, with positive ε_{Hf-Nd} at 2.98 Ga, reinforce the Early Mesoarchean as the main crustal growth period in the province. In addition, we propose that the differentiation of the depleted mantle (DM) beneath the Carajás Province may have initiated around 3.8 Ga.

Keywords: Mesoarchean TTGs; Carajás Province; Amazonian Craton; U-Pb geochronology; Hf-Nd isotopes

Check for updates

Academic Editor: Dmitry Konopelko

Received: 25 February 2026
Revised: 23 April 2026
Accepted: 26 April 2026
Published: 2 May 2026

1. Introduction

The end of the Archean is considered a period of major geodynamic changes on Earth [1–6]. As the planet cooled and differentiated, continental crust was progressively extracted from the mantle, and up to half of its present volume may have formed before 2.9 Ga [7–10]. Archean crust is commonly described as consisting of granite–greenstone terranes dominated by tonalite–trondhjemite–granodiorite (TTG) suites [11–13]. The geodynamic evolution of the Archean remains debated, particularly regarding how and when "modern-style" plate tectonics began [1,14–19]. Two main tectonic models have been proposed: one dominated by vertical tectonics (sagduction; refs. [4,18,20–23]) and another involving subduction-related processes [1,14,19,22–27].

In the southeastern Amazonian Craton, the Carajás Province (CP) represents the oldest and best-preserved crustal domain of the Central Brazil Shield (Figure 1A,B). In most tectonic models, the CP is subdivided into the Meso- to Neoarchean Carajás Domain (CD) to the north and the Mesoarchean Rio Maria Domain (RMD) to the south [28,29].

The Serra do Inajá region, the focus of this study, corresponds to the southernmost portion of the RMD (Figure 1C) and represents its least studied area in terms of geological and geochronological data, mainly due to limited access. Vasquez and Rosa-Costa [29] compiled the available field, petrological, and geochronological information, establishing a lithostratigraphic and geotectonic framework for the region. More recently, the Geological Survey of Brazil (SGB/Belém) conducted a mapping project focused on RMD greenstone belts, and Silva et al. [30] published an updated geological map including the Serra do Inajá region. Despite these advances, geochronological and geochemical datasets remain limited, hindering correlations with other parts of the RMD and broader geodynamic interpretations within the CP.

Several key questions remain unresolved, particularly regarding the timing of Mesoarchean magmatic events and their relationships with thermo-tectonic processes. While these events are well constrained in the Xinguara and Rio Maria regions (northeastern RMD) [31–33], the southern extent toward the Serra do Inajá region remains unclear. The nature and sources of magmatism, as well as their relationships with greenstone belts and tectonic setting, are still poorly constrained, limiting interpretations of granitoid genesis and emplacement environments. For instance, it remains unclear whether a dome-and-keel model followed by Archean subduction would be applicable to the entire RMD [4,34].

The age and nature of the primitive continental crust in the RMD also remain debated. Whole-rock Nd-T_{DM} ages from the CP range between 2.9 and 3.3 Ga [35–41], suggesting a major Mesoarchean crustal growth episode [32,33,42–44]. Zircon Lu–Hf data indicate Hf crustal model ages (Hf-T_{DM}^{C}) between 3.6 and 3.0 Ga for mafic and felsic rocks, supporting a Meso- to Paleoarchean crustal growth event [38,40,45–48], while detrital zircon data suggest the presence of Eoarchean remnants [49]. In the RMD, Lu–Hf data from zircon of Orosirian granites (Hf-T_{DM}^{C} = 3.9–3.1 Ga) indicate derivation from older Meso- to Paleoarchean TTGs [37,48]. However, no zircon Lu–Hf data are currently available for Archean rocks of the RMD.

This study presents new petrographic, geochemical, and geochronological data for granitoids of the Mesoarchean Arco Verde Complex (AVC) in the Serra do Inajá region. This unit records the oldest magmatic event in the RMD and thus represents a key component for understanding the early formation of the Archean crust in the region and within the Amazonian Craton. We provide detailed petrographic and geochemical analyses to investigate the nature of magmatism and its tectonic setting. U–Pb zircon dating of two granodiorites confirms the Mesoarchean crystallization age of the AVC. Additionally, we present the first zircon Lu–Hf data for the RMD basement, together with whole-rock Sm–Nd data, to constrain crustal growth episodes and compare them with the Hf–Nd dataset of the CP. Finally, the timing of depleted mantle differentiation beneath the CP is evaluated.

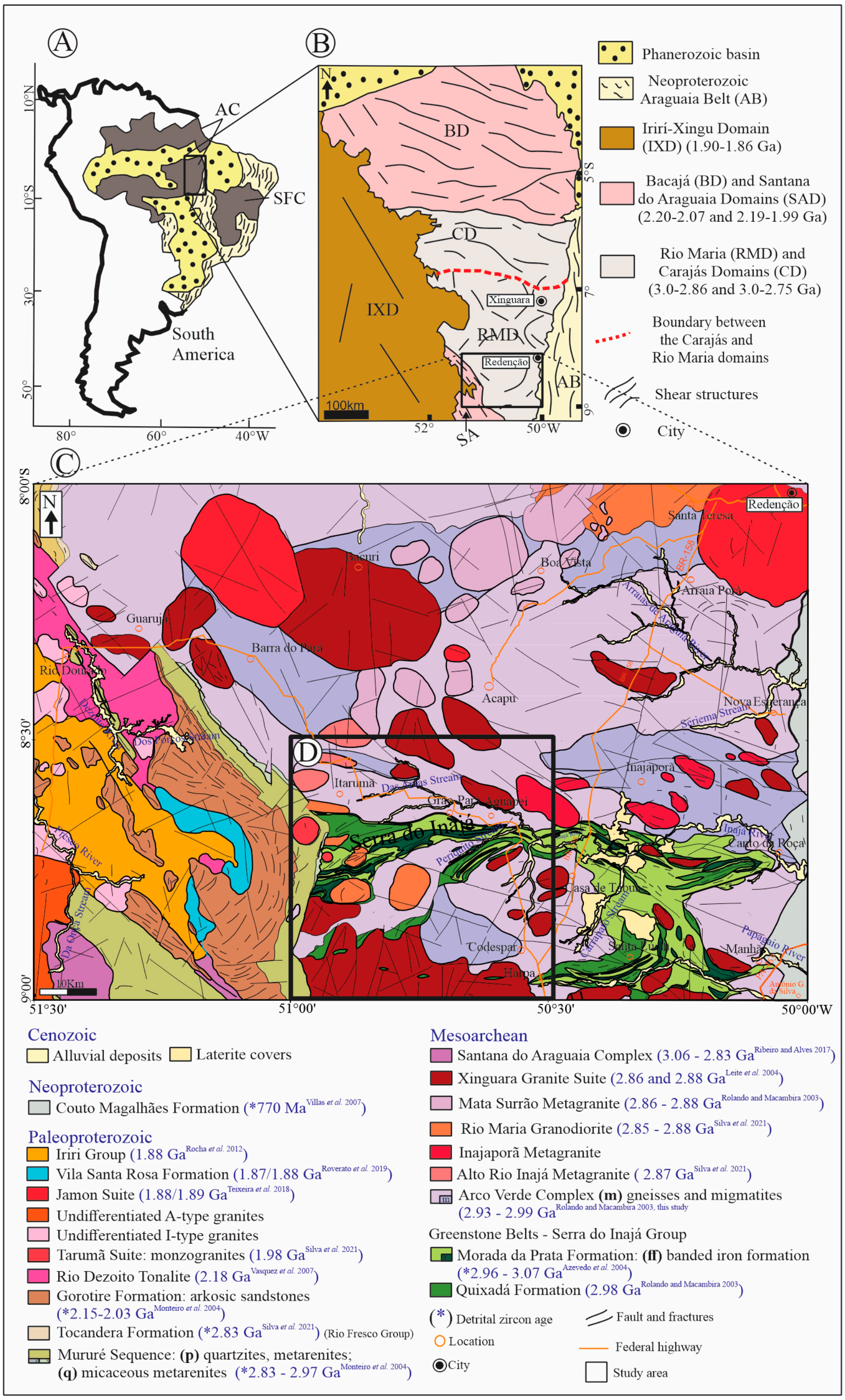

Figure 1. (**A**) Simplified geological map of Brazil on the South American continent (AC: Amazonian Craton. SFC: São Francisco Craton). (**B**) Main geological domains of the southeastern Amazonian Craton (modified from [50]). The map shows the Archean Carajás province with the Rio Maria and Carajás domains limited by the dashed line. Adjacent domains are the Siderian-Rhyacian Bacajá domain (BD) to the north, the Orosirian Iriri-Xingu domain (IXD) to the west, the Rhyacian Santana do Araguaia domain (SAD) to the south, and the Neoproterozoic Araguaia Belt (AB-Tocantins Province) to the east. (**C**) Simplified geological map of the Serra do Inajá region, southern portion of the Rio Maria Domain, (**D**) Southwest area of Serra do Inajá region, the object of this study, modified from [30]. Geochronological references: [30,31,33,46,51–57].

2. Geological Setting

The Amazonian Craton comprises Archean microcontinents surrounded by Paleoproterozoic and Mesoproterozoic accretionary orogenic belts and was stabilized in the early Neoproterozoic, with limited influence from younger orogens (Figure 1A) [58].

The Carajás Province (CP) represents the only preserved Archean nucleus within the craton [58]. It is bounded by the Paleoproterozoic Santana do Araguaia (SAD) and Iriri–Xingu (IXD) domains to the southwest, the Neoproterozoic Araguaia Belt (AB) to the southeast, and the Paleoproterozoic Bacajá Domain (BD) to the north (Figure 1B) [29]. In current tectonic models, the CP is included within the Central Amazonian Province together with the Xingu–Iricoumé domain [41]. It is subdivided into the Rio Maria Domain (RMD; 3.0–2.86 Ga) and the Carajás Domain (CD; 3.07–2.70 Ga), separated by major E–W shear zones [29]. A single Proterozoic magmatic event is recorded at ca. 1.88 Ga, marked by the emplacement of Orosirian anorogenic granites [37,46,48,59].

The RMD is a typical granite–greenstone terrane composed of TTG suites, greenstone belts, sanukitoid-like granitoids, and high Ba–Sr- and K-rich granitoids [31,32,38,44,45,47,60–64]. It consists of dome-like granitoid bodies surrounded by arcuate belts of low-grade metavolcanic and metasedimentary rocks and was largely stabilized by the end of the Mesoarchean. In contrast, the CD records intense Neoarchean magmatism, deformation, and basin development and is subdivided into the Sapucaia Subdomain, the Canaã dos Carajás Subdomain, and the Carajás Basin [44,45,65–69].

The Carajás Basin comprises Neoarchean metavolcano–sedimentary sequences (2.78–2.55 Ga) overlain by Paleoproterozoic sedimentary rocks [29,61,70,71]. The Canaã dos Carajás Subdomain represents its Mesoarchean basement and is marked by the Neoarchean E–W Itacaiúnas Shear Zone, with predominance of granitoids, migmatites, granulites, and charnockites, and scarce TTGs [46,51,72–74]. The Sapucaia Subdomain, located between the RMD and CD, includes greenstone sequences, TTGs, and calc-alkaline granitoids (2.95–2.84 Ga) and may represent a reworked extension of the RMD affected by Neoarchean tectono-magmatic events [28,39–41,51,74–78].

The RMD preserves Mesoarchean magmatic units with limited overprint from Neoarchean events. The oldest rocks include the Arco Verde Complex (2.98–2.92 Ga) and greenstone belts (~3.06–2.90 Ga), composed mainly of metaultramafic and metamafic rocks with subordinate felsic units and metasediments [50,79–81]. The Serra Azul ultramafic complex (2.97 Ga) is coeval with these sequences [63,81]. The Archean evolution of the RMD involved two main tectono-magmatic stages: (i) 2.98–2.92 Ga, marked by subduction-related processes, including slab melting and mantle metasomatism; and (ii) ca. 2.87 Ga, characterized by granitoid emplacement in a collisional setting, involving crustal reworking, transpressive shear zones, and magma interaction [31,44–46,59,82]. These processes are commonly interpreted in accretionary–collisional frameworks, although alternative models invoke vertical tectonics (e.g., sagduction and drip tectonics), consistent with the dome-and-keel architecture of the RMD [31,35,40,46,83]. Archean plutonic rocks in the RMD are grouped into four granitoid suites: (I) TTG and trondhjemitic rocks (2.98–2.93 Ga), including the Arco Verde tonalite, which represent the most voluminous units; (II) moderate- to high-K calc-alkaline granitoids, including sanukitoids (2.89–2.82 Ga); (III) biotite metagranites (2.91–2.86 Ga); and (IV) high-K, Ba–Sr granitoids (2.87–2.86 Ga) [30–33,45,46,52–57,82–89]. In the southern RMD (Figure 1C), Suite I is represented by the Arco Verde Complex, whereas Suite II includes the Rio Maria sanukitoids and the Alto Rio Inajá and Inajaporã metagranites, and Suite III includes the Xinguara and Mata Surrão granitoids.

In the northern RMD, the Arco Verde tonalite forms batholiths that dominate the region. It consists of isotropic to foliated, medium- to coarse-grained rocks with common compositional banding, showing increasing deformation toward shear zones, while igneous textures are locally preserved [28]. Foliation is typically subvertical and roughly E–W-oriented (WNW–ESE to WSW–ENE), recording progressive deformation from synmagmatic to subsolidus conditions during cooling. Enclaves and aplitic to pegmatitic veins are common. Geochemically, these rocks display typical TTG signatures (high Al_2O_3 and Na_2O, low Y and Yb) and were likely derived from partial melting of garnet amphibolites related to tholeiitic or greenstone belt protoliths [90].

In the southern RMD, the AVC has been considered equivalent to the Arco Verde tonalite and comprises metatonalites, metatrondhjemites, and metagranodiorites associated with a significant unit of migmatized and/or foliated orthogneisses, which justifies its designation as a complex (Figure 1D) [37]. These rocks display lithological and structural features comparable to those observed in the northern sector. Geochronological data for the main Archean to Paleoproterozoic units of the RMD are summarized in Table 1.

Table 1. Compilation of U-Pb zircon ages and Sm-Nd and Lu-Hf isotopic data of the Mesoarchean and Paleoproterozoic units of the Rio Maria Domain.

Unit/Lithology	Zircon U–Pb Age (Ma)	Zircon Pb–Pb Age (Ma)	WR Nd-T_{DM} (Ga)	$\varepsilon_{Nd(t)}$	Zircon Hf-T_{DM}^{C} (Ga)	Zircon $\varepsilon_{Hf(t)}$
Mesoarchean						
Calc-alkaline magmatism						
Xinguara Metagranite		2865 ± 1 [31]	2.9 [91]	+1.6		
Manelão Granite	2905 ± 12 [30]					
Mata Surrão Granite		2868 ± 5, 2871 ± 7, 2875 ± 11, 2881 ± 2 [33,83,92]				
Guarantã Granite	2870 ± 16 [63]	2868 ± 5, 2864 ± 8 [63,92]				
Trairão Granodiorite	2872 ± 7, 2869 ± 12 [63]					
Rio Maria Granodiorite	2872 ± 5, 2874 + 9 [84,85]	2878 ± 4, 2877 ± 6, 2880 ± 4 [33,93]	2.9 to 3.1 [42,91]	+2 to +1.2		
Cumaru Granodiorite		2817 ± 4 [66]				
Parazônia Quartz Diorite		2876 ± 2 [67]				
Rio Maria Quartz diorite		2878 ± 4 [93]				
Rancho de Deus Granite	2898 ± 61 [63]					
Tucumã Granite	2844 ± 8, 2859 ± 4 [68]					
Sodic magmatism						
Bonito Granodiorite	2870.6 ± 4 [69]					
Mogno Trondhjemite	2972 ± 9, 2961 ± 16, 2924 ± 19 [32]	2959 ± 5 [32]	2.9–3.1 [32]	+2.0 to +2.5		
Carapanã Tonalite	2917 ± 9, 2923 ± 9 [68]					
Mariazinha Tonalite	2912 ± 5 [32]	2925 ± 3, 2924 ± 2 [32]	2.9 [32]	+1.9		
Arco Verde Complex	2941 ± 5, 2957 ± 25, 2948 ± 4, 2979 ± 4 [30,32,85]	2964 ± 4, 2948 ± 7, 2981 ± 8 [33,92]				
Mafic–ultramafic magmatism						
Serra Azul Complex	2970 ± 7 [84]					
Greenstone Belts						
Igarapé da Pista Formation	3063–2944 [30]		3.4 [70]	−0.34		
Igarape Abelha Formation	2979 ± 23, 2996 ± 5 [30]					
Babaçu Formation	3046 ± 32 (WR) [61]			+1.1 to +2.5 [61]		
Lagoa Seca Formation	2904 + 29/−22, 2971 ± 18, 2979 ± 5 [71,72,84,85]	2943 ± 88 [61]	3.1–3.2 [61]	+0.2 to +3.1		
Lagoa Seca Formation	3050, 3200, 3400, 3700 (DZ) [73]					
Morada da Prata Formation		2960–3070 (DZ) [51]				
Quixadá Formation	2988 ± 4 [33]		3.02 [33]	+1.6 to +5.7		
Paleoproterozoic						
Intraplate magmatism						
Jamon Granite	1885 ± 32 [46]	1885 ± 32 [93]	2.9–3.0 [42,93]	−9.7 to −9.5	3.3–3.5 [37]	−12 to −15.7
Musa Granite	1883 + 5, 1882 ± 4 [93]		2.6–2.8 [42,93]	−9.3 to −9.6		
Redenção Granite	865 ± 6, 1871 ± 5, 1883 ± 9 [46]	1870 ± 68 (WR) [74]			3.3–3.5 [37]	−13.6 to −14.9
Redenção Granite	1902 ± 27 (Ttn) [46]					
Bannach Granite	1857 ± 14, 1874 ± 6 [46]		2.8 [37]	−9.6	3.1–3.2 [37]	−11 to −9.3
Gradaús Granite		1882 ± 9 [78]				
Manda Saia Granite	1864 ± 6.5, 1866 ± 10 [48,94]		2.6–2.7 [94]	−8.1 to −8.4	3.2–3.6 [48]	−12.9 to −18.7

Table 1. *Cont.*

Unit/Lithology	Zircon U–Pb Age (Ma)	Zircon Pb–Pb Age (Ma)	WR Nd-T_{DM} (Ga)	$\varepsilon_{Nd(t)}$	Zircon Hf-$T_{DM}{}^{C}$ (Ga)	Zircon $\varepsilon_{Hf(t)}$
Marajoara Granite	1885 ± 6, 1887 ± 8, 1884 ± 11 [40,94,95]				2.9–3.0 [82]	−11.3 to −17.9
Felsic dykes	1880 ± 3, 1881 ± 4 [96]	1885 ± 2 [59,93]	2.8–2.9 [42,93]	−9.4 to −10		
Seringa Granite	1875 ± 6, 1879 ± 18, 1880 ± 7, 1889 ± 8 [46]	1895 ± 1, 1892 ± 3 [97,98]			3.3–3.6 [37]	−12.8 to −17.3
São João Granite	1876 ± 12, 1878 ± 3, 1880 ± 3, 1891 ± 5 [46]	1890 ± 2 [86]			3.4–3.9 [37]	−24.2 to −12.9
Velho Guilherme Granite	1853 ± 6, 1882 ± 6 [46,80]	1873 ± 13 (WR) [81]				
Sedimentary cover						
Gorotire Formation		2154 ± 9 to 2035 ± 5 (DZ) [97]				
Cachoeirinha Formation	2760–3150 (DZ) [72]					
Tocandeira Formation		2830 (DZ) [30]				

Legend: WR = whole rock; DZ = detrital zircon; Ttn = titanite.

3. The Serra do Inajá Region

The study area corresponds to the southwestern part of the Serra do Inajá region (Figure 1D). It is bounded to the west by Paleoproterozoic units of the SAD, including: (i) the Mururé Formation (metapelites, slates, metarenites, and quartzites) and the Gorotire Formation (arkosic sandstones and quartzites), with maximum depositional Pb evaporation ages on detrital zircon of ~2.83 Ga and ~2.03 Ga, respectively [56]; and (ii) the Tarumã Suite monzogranite (1.98 Ga; ref. [30]), which intrudes the Mururé Formation. To the east, the area is bounded by the passive-margin sedimentary sequence of the AB (Couto Magalhães Formation) [30].

As in the entire RMD, Mesoarchean units predominate, forming a typical granite–greenstone terrane. The region is characterized by a pervasive foliation with a general E–W orientation, locally varying to WNW–ESE, WSW–ENE, NE–SW, and more rarely N–S. Greenstone belts form extensive, continuous bands surrounding rounded to slightly elongated granitoid bodies of the AVC (Figure 2). Dome-shaped TTG batholiths enclosed by metavolcano–sedimentary keels define a typical dome-and-keel architecture. Lineations display a concentric pattern with down-dip orientations relative to foliations, suggesting structural development linked to vertical tectonics in the Serra do Inajá region [30].

The greenstone sequences belong to the Serra do Inajá Group and include the Quixadá and Morada da Prata formations. The Quixadá Formation (lower unit) comprises metabasalts, ultramafic schists, metaperidotites, metapyroxenites, and banded iron formations. A metabasalt yielded a zircon ID-TIMS age of 2988 ± 4 Ma and a Nd-T_{DM} model age of 3.02 Ga, with ε_{Nd} values from +1.7 to +5.8 [33]. The Morada da Prata Formation (upper unit) consists of phyllites, metarenites, carbonaceous metaschists, metasiltites, banded iron formations, and rare metadacites. Pb–Pb dating of detrital zircon yielded ages between 2.96 and 3.07 Ga, constraining a maximum depositional age of 2.96 Ga [51].

The AVC (Figure 2) is the predominant unit and is mainly composed of tonalites, granodiorites, and trondhjemites. Gneisses and migmatites metamorphosed under amphibolite facies also occur, particularly in the southwestern area. These rocks form large batholiths intruded by younger Mesoarchean and Orosirian granitoids [30]. The only geochronological data available for the AVC in the study area is a U–Pb zircon age of 2988 ± 5 Ma from a tonalite [33]. In areas to the north, however, several AVC units have been dated by SHRIMP, LA-ICP-MS, ID-TIMS U–Pb, and Pb–Pb zircon methods, yielding ages between 3.02 and 2.91 Ga and ε_{Nd} values between +1.6 and +2.6 (Table 1; refs. [29,30,32,33,42,92]).

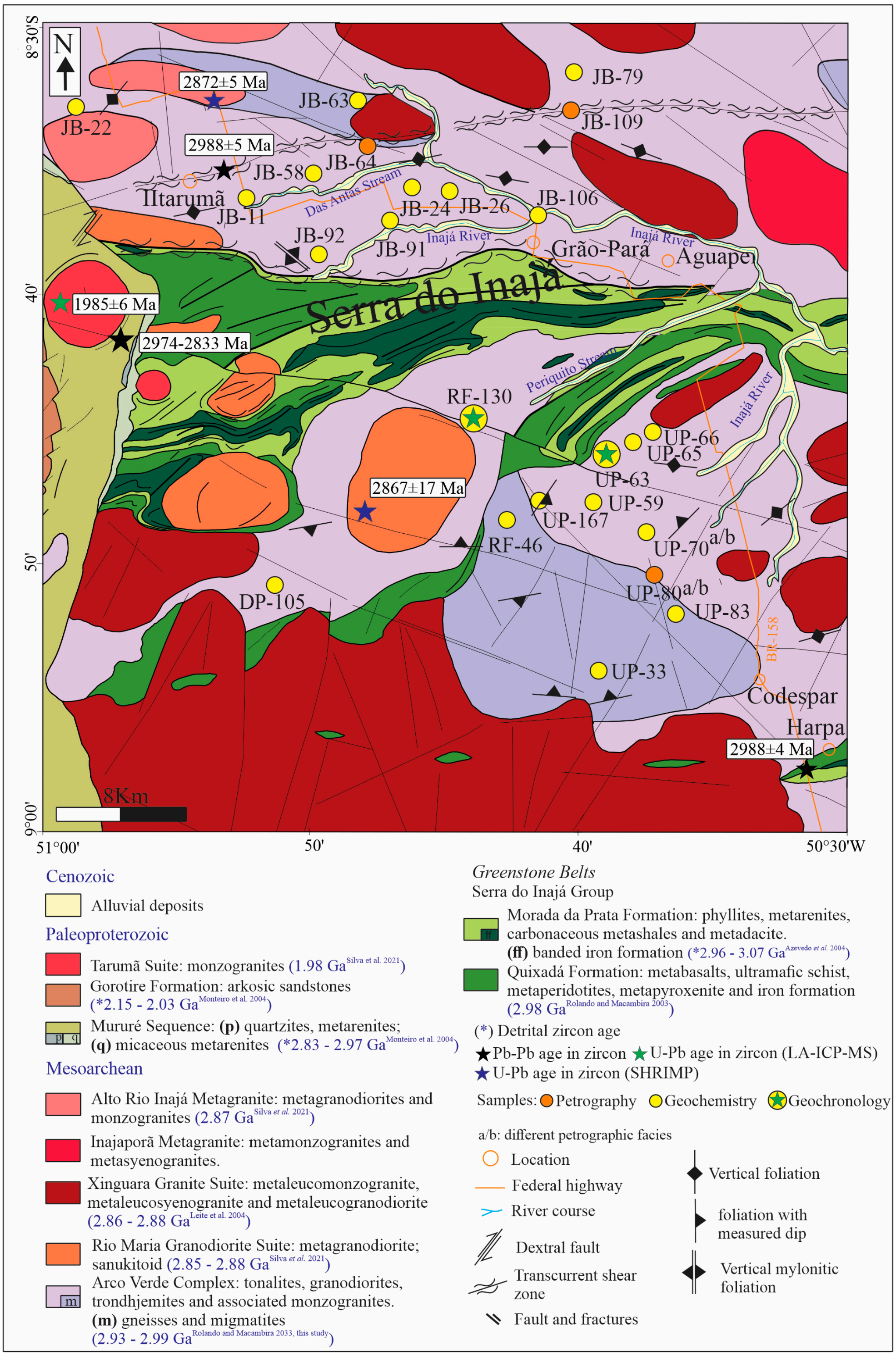

Figure 2. Geological map of the study area, southwest of the Serra do Inajá region, with a sample of the AVC granitoids. Modified from [30]. Geochronological references: [30,31,33,51,56].

In the central part of the area, the Rio Maria Suite (2867 ± 17 Ma; ref. [30]) intrudes both the greenstone belts and the TTG granitoids of the AVC. The second largest mappable unit is the Xinguara Metagranite (Xinguara Suite), composed of metagranodiorites, metaleucosyenogranites, and subordinate metaleucomonzogranites [31]. It displays weak foliation, becoming more penetrative toward the margins, especially near contacts with country rocks. Although not dated locally, a Pb–Pb zircon age of 2865 ± 1 Ma has been reported for a northern occurrence [31].

In the northwestern portion, the Alto Rio Inajá Metagranite (2872 ± 5 Ma; ref. [30]) consists of metagranodiorites and metamonzogranites forming E–W elongated elliptical bodies, with good exposures as boulders and slabs, and intrudes the AVC ([30]; Figure 2). In the northeastern portion, the Inajaporã Metagranite, composed of metamonzogranites and metasyenogranites, also intrudes the AVC and is characterized by high Th and U contents and intermediate K contents, as indicated by aerogeophysical data. These rocks do not show distinctive topographic or magnetic features that clearly differentiate them from the host units [30].

4. Materials and Methods

Twenty-six samples from the AVC were selected for this study, kindly provided by SGB/Belém. These samples are part of the Geological–Geophysical–Metallogenetic Integration Project of the Greenstone Belts Sequences of the Rio Maria Domain—New Frontiers Rio Maria [30]). The sampling strategy was designed to cover the main lithotypes of the AVC and ensure representative petrographic, geochemical, and isotopic characterization across the study area. It complements the dataset of the SGB/Belém study, which includes geochemical analyses of 24 samples, by improving lithological and spatial coverage. Most samples were collected from areas where granitoids occur; additionally, four samples were also selected from orthogneiss and migmatite domains identified by [30]. Sampling was guided by lithotype distribution and spatial representativeness. However, it was locally constrained by limited outcrop exposure and difficult access in this remote region. Twenty-three petrographic analyses were conducted using a conventional petrographic optical microscope at the Petrography Laboratory (LAPETRO) of the Graduate Program in Geology and Geochemistry (PPGG) at the Institute of Geosciences (IG), UFPA. Modal counting was performed on 2800 points with a 2-point spacing, using a Swift point counter. For whole-rock geochemistry, the analyses of twenty-one samples were performed in a commercial laboratory (ALS Geochemistry Laboratories Ldta). Major elements were analyzed by ICP-ES (Inductively Coupled Plasma-Emission Spectrometry), and trace elements, including rare earth elements, were analyzed by ICP-MS (Inductively Coupled Plasma-Mass Spectrometry). Two of these samples were used for zircon U−Pb/Lu−Hf and whole-rock Sm-Nd geochronology. The in situ analyses were performed at the UFPA Isotope Geology Laboratory (Pará-Iso) with a Thermo Finnigan Neptune inductively coupled plasma mass spectrometer equipped with nine Faraday collectors and six multiplier ion counters (MC-ICP-MS). The laser microprobe (LA) coupled to the MC-ICP-MS was a CETAC LSX-213 G2 device. Details on the analytical procedures for U-Pb and Lu-Hf in zircon are found in [87] and Supplementary Material. The whole-rock Sm-Nd analyses were performed at the Geochronology Laboratory of the University of Brasília (UnB), and the whole-rock Sm-Nd analytical procedures have been described in [88]. For the Hf-$T_{DM}{}^{C}$ model age calculation, an age of 3.8 Ga, suggested by [89], has been used for the differentiation of the Depleted Mantle, instead of the 4.56 Ga evolution trend proposed by [99]. A comprehensive description of the analytical procedures for petrography, whole-rock geochemistry, and U−Pb, Lu−Hf and Sm-Nd geochronology is presented in the Supplementary Material.

5. Results

5.1. Field Aspects and Petrography

In the field, granitoids belonging to the Serra do Inajá region (in Figure 3A—a view of the mountain range) are present in outcrops that can vary from slabs to boulders (examples in Figure 3B,C). The AVC rocks present four distinct lithotypes (Figure 4) with a mineralogical composition of tonalite (Figure 5A), granodiorite (Figure 5D) and monzogranite (Figure 5G) in the QAP diagrams (Figure 4), including orthogneisses with tonalitic protoliths (Figure 5J).

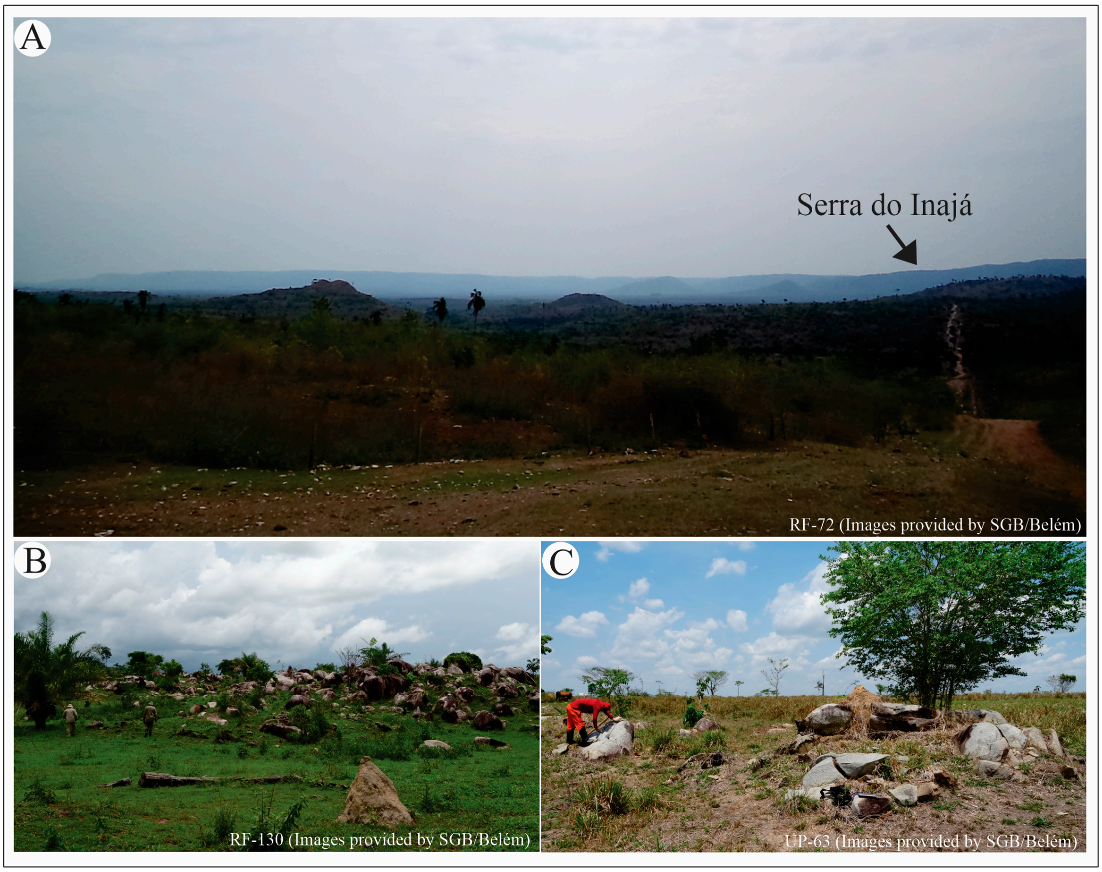

Figure 3. Illustration of the current types of outcrops present in the Inajá region. (**A**) View of Serra do Inajá, point of sample RF-72; (**B**) Outcrops in boulders, from sample RF-130; and (**C**) Outcrops in flagstones and boulders, from sample UP-63. Images provided by SGB/Belém.

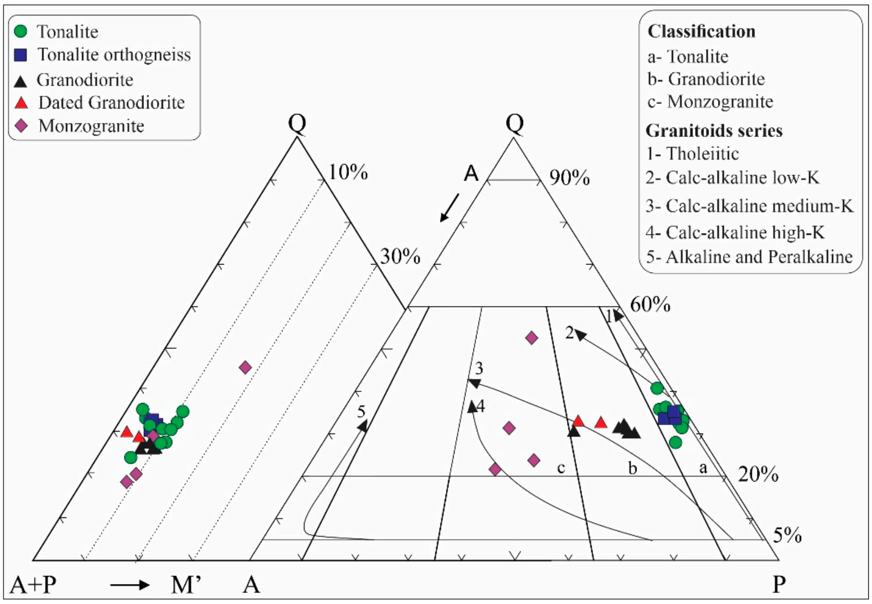

Figure 4. Modal composition Q-A-P [100] and Q-(A + P)-M [101] diagrams for the granitoids and orthogneisses of the AVC. Q—quartz; A—alkali feldspar; P—plagioclase; M—mafic minerals. The black arrows represent the trends of the granitoid series.

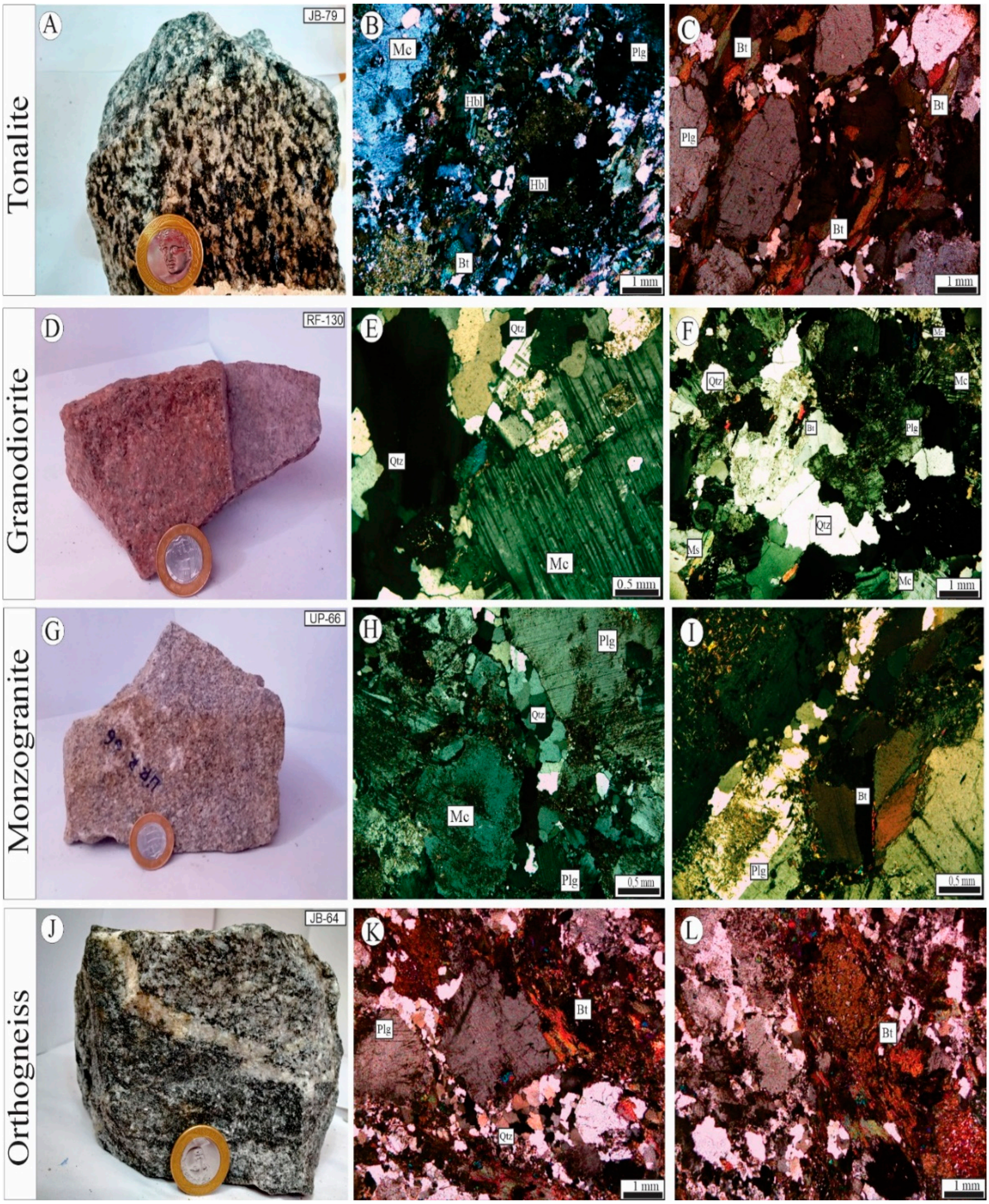

Figure 5. (**A**) Tonalite (hand sample); (**B**) symplectites (PL); (**C**) recrystallized quartz and weakly oriented biotite (PL); (**D**) granodiorite (hand sample); (**E**) hypidiomorphic granular texture of granodiorite (PL); (**F**) main mineral assemblage of granodiorite (PL); (**G**) monzogranite (hand sample); (**H**) main mineral assemblage of monzogranite (PL); (**I**) detail of biotite (PL); (**J**) tonalitic orthogneiss (hand sample); (**K**) stretching of minerals defining the gneissic fabric (PL); (**L**) comminution textures. PL = polarized light. Mineral abbreviations after [102].

The four lithotypes are mainly composed of plagioclase (An22–33), quartz, and microcline (Figure 5B,E,H). Ferromagnesian minerals include hornblende and biotite, the latter present in all lithotypes (Figure 5C,I). Modal proportions of essential, accessory, and secondary minerals are given in Supplementary Table S1.

Tonalites, granodiorites, and monzogranites exhibit hypidiomorphic granular textures with incipient deformation, expressed by crystal stretching and comminution. Plagioclase shows albite and albite–Carlsbad twinning and is commonly altered to sericite, clay minerals, and epidote. Myrmekitic textures occur at grain boundaries in contact with quartz (Figure 5H). Microcline displays tartan twinning, local perthitic textures, and alteration to clay minerals. Quartz occurs as hypidiomorphic crystals with undulose extinction and as recrystallized aggregates (Figure 5I).

Biotite is moderately chloritized and forms aggregates with titanite, opaque minerals, magmatic epidote, allanite, and minor hornblende, which is more abundant in tonalites. Symplectitic textures are observed in tonalitic sample JB-79 (Figure 5B). Biotite also occurs in stretched and strongly chloritized domains (Figure 5C). Plagioclase and microcline locally show corrosion and intense alteration (saussuritization; Figure 5K). Quartz recrystallization and weak biotite orientation are also observed (Figure 5C).

Orthogneisses display granoblastic to granolepidoblastic textures, with well-developed foliation and gneissic banding. In some domains, mylonitic textures with intense grain-size reduction are observed (Figure 5K,L), indicating stronger deformation relative to the other lithotypes. Sample JB-64 shows a comminuted crystalline network, interpreted as related to shear zone deformation. Accessory minerals include titanite, epidote, apatite, zircon, and opaques. Secondary muscovite occurs in some biotite monzogranites and rarely in tonalites. Other alteration products include sericite, clay minerals, carbonates (saussuritization), and chlorite.

Orthogneisses exhibit compositional banding at millimetric to centimetric scale, defined by alternating quartz-feldspathic and biotite–amphibole-rich layers. Enclaves of quartz diorite, amphibolite, and leucomonzogranite are common, as well as aplitic and pegmatitic veins, concordant or discordant with foliation. Foliation trends predominantly E–W, varying between WNW–ESE and WSW–ENE [36]. Rocks are generally equigranular, medium- to coarse-grained, with hypidiomorphic granular textures and composed of plagioclase, microcline, quartz, biotite, and hornblende (Figure 5A,E,I).

Silva et al. [30] describe the southern RMD as dominated by banded, foliated, and locally migmatized orthogneisses of tonalitic to granodioritic composition, commonly containing mafic enclaves. Metamorphism reached amphibolite facies conditions. These rocks are typically associated with contacts of the Xinguara and Rio Maria suites and with shear zones, where deformation is more intense and mylonitic textures are developed.

5.2. Geochemistry

Tonalites are intermediate to acidic rocks, with SiO_2 contents ranging from 61.5 to 74.4 wt%. They are characterized by high Na_2O (3.96–5.16 wt%) and low K_2O (1.17–2.42 wt%) contents, resulting in K_2O/Na_2O ratios between 0.26 and 0.61. Magnesium-number (Mg# = molar MgO/[MgO + FeO*]) values are moderate, varying from 0.28 to 0.51. The compositions of the granodiorites and monzogranites partially overlap those of the tonalites in terms of SiO_2 content (73.0–75.7 wt%) but differ by lower Mg# values (0.15–0.27) and higher K_2O/Na_2O ratios (0.61–1.14). The data can be verified in greater detail in Supplementary Table S2.

In the P-Q cationic classification diagram [103], the samples plot within the tonalite, granodiorite, and granite fields. Tonalite samples follow the tholeiitic trend, whereas the more evolved samples display an evolutionary trend comparable to that of the sodic subalkaline series (Figure 6A). Similarly, in the normative Ab-Or-An diagram of [104], with fields after [105], the samples plot within the tonalite, trondhjemite, granodiorite, and granite fields (Figure 6B).

https://doi.org/10.3390/min16050483

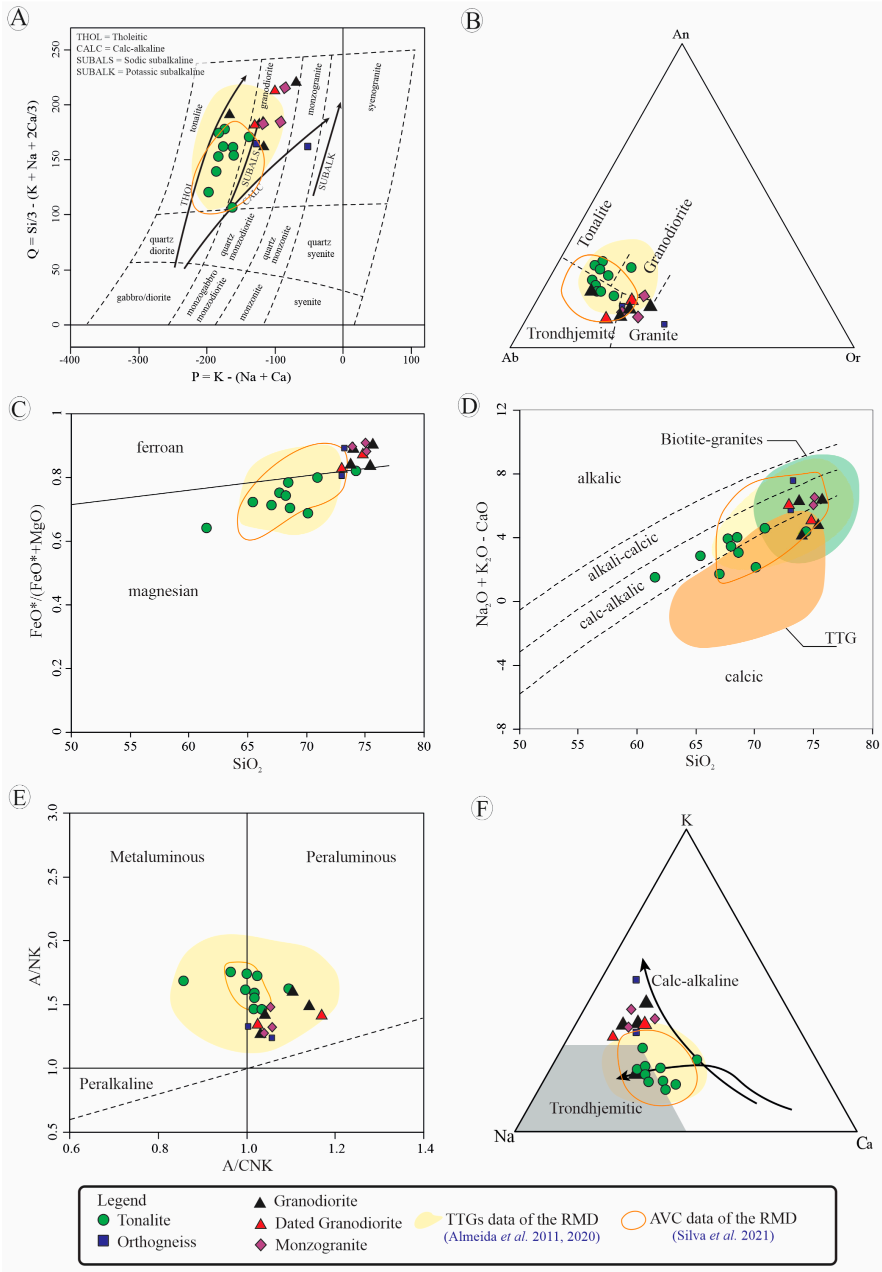

Figure 6. Geochemical diagrams of major elements for the AVC TTGs, granitoids and orthogneisses, from the southern part of the Serra do Inajá region: (**A**) P-Q diagram from [103]; (**B**) Feldspar classification ternary diagram [104]; (**C**) SiO_2 vs. FeOt/FeOt + MgO diagram [106]; (**D**) index diagram MALI ([Na_2O + K_2O] − CaO) vs. SiO_2 [106]; (**E**) Alumina saturation index diagram [90]; and (**F**) Na-K-Ca ternary diagram for the calc-alkaline (CA) and trondhjemite (Tdh) series, as defined by [11]. Comparative data references: [30,32,64].

According to the SiO_2 vs. FeO*/(FeO* + MgO) diagram [106], all tonalite samples are magnesian, with Fe-number values ranging from 0.64 to 0.82. In contrast, the granodiorites and monzogranites are relatively Fe-rich (0.81–0.91) and plot in the ferroan field (Figure 6C). In the SiO_2 vs. $Na_2O + K_2O + CaO$ diagram [106], all samples exhibit transitional behavior between the calcic and calc-alkalic fields, except for the orthogneiss UP-70A, which plots within the alkali-calcic field (Figure 6D).

Regarding the alumina saturation index [90], the granitoids are metaluminous to slightly peraluminous, with A/CNK (A/CNK = molar $Al_2O_3/[CaO + Na_2O + K_2O]$)

values ranging from 0.86 to 1.10. Only two biotite granodiorite samples (UP-65 and RF-130) deviate from this range, with A/CNK values of 1.14 and 1.17, respectively (Figure 6E).

In the AFM diagram [107], all rock groups plot within the calc-alkaline domain, with the most differentiated samples clustering near the A apex (Figure 6F). A calc-alkaline affinity is also indicated in the SiO_2 vs. K_2O diagram [108], where most samples fall within the medium-K calc-alkaline field (Figure 7G).

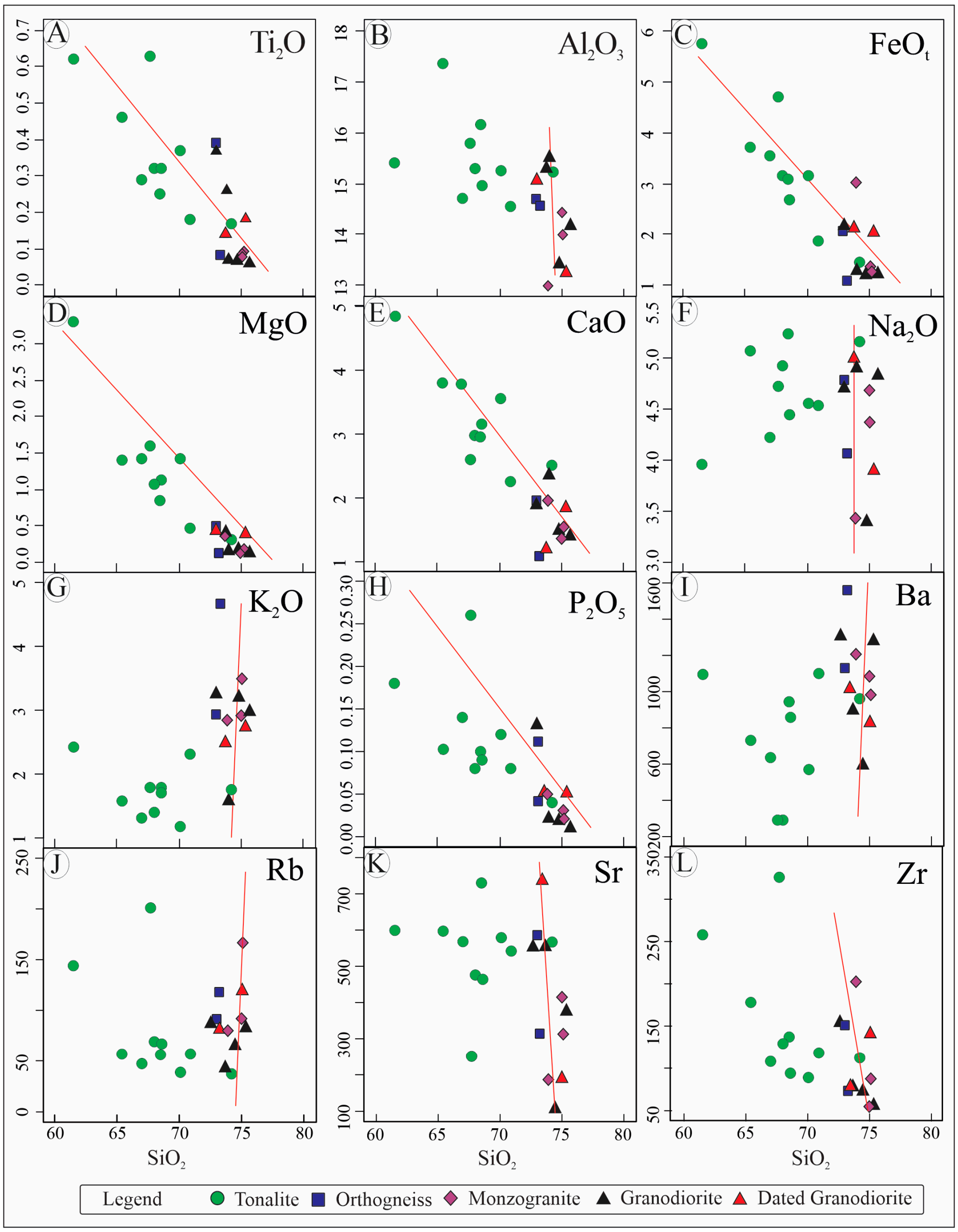

Figure 7. Major element (in wt%) Harker diagrams for the Granitoids of the AVC from the southern part of the Serra do Inajá region. Fields in accordance with [108]: (**A**) TiO_2 vs. SiO_2; (**B**) Al_2O_3 vs. SiO_2; (**C**) FeOt vs. SiO_2; (**D**) MgO vs. SiO_2; (**E**) CaO vs. SiO_2; (**F**) Na_2O vs. SiO_2; (**G**) K_2O vs. SiO_2; (**H**) P_2O_5 vs. SiO_2; (**I**) Ba vs. SiO_2; (**J**) Rb vs. SiO_2; (**K**) Sr vs. SiO_2; (**L**) Zr vs. SiO_2.

In the Na-K-Ca ternary diagram [11], tonalites plot mainly along the trondhjemitic trend, near the Na apex, overlapping the trondhjemitic affinity field [12]. In contrast, granodiorites and granites define a vertical trend of K enrichment that is parallel to the calc-alkaline trend (Figure 6F).

In Harker diagrams, tonalites, granodiorites, and monzogranites generally plot along a common evolutionary trend marked by decreasing TiO_2, FeO*, MgO, CaO, and P_2O_5 with increasing SiO_2. These trends suggest that fractional crystallization of amphibole, biotite, titanite, and apatite played an important role in the petrogenetic evolution of the different rock groups (Figure 7A–H). However, significant differences are observed in the Al_2O_3, Na_2O, and K_2O versus SiO_2 diagrams, where granodiorites and monzogranites define approximately subvertical evolutionary trends. Such patterns cannot be explained solely by fractional crystallization and suggest the involvement of additional petrogenetic processes, such as partial melting and/or magma mixing. Bivariate diagrams involving trace elements (e.g., Ba, Rb, Sr, and Zr) show similarly steep trends, reinforcing the interpretation that multiple differentiation mechanisms operated during magma evolution (Figure 7I–L). In contrast, tonalites display a more scattered distribution relative to SiO_2, suggesting greater compositional heterogeneity or a weaker degree of magmatic differentiation.

In Harker diagrams, tonalites, granodiorites, and monzogranites generally plot along a common evolutionary trend, marked by decreasing TiO_2, FeO*, MgO, and CaO with increasing SiO_2. However, plots of Al_2O_3, Na_2O, and K_2O against SiO_2 show that granodiorites and monzogranites define steeper trends than those of tonalites, suggesting that different petrogenetic processes operated within each rock group (Figure 7A–H).

Regarding trace elements, no clear correlations with SiO_2 are observed in the Harker diagrams. Large-ion lithophile element (LILE) concentrations overlap widely across the different rock groups. Nevertheless, tonalites are enriched in Sr (537 ppm on average) and depleted in Rb (77 ppm on average) and Ba (748 ppm on average) relative to granodiorites and monzogranites (averages of Sr = 393 ppm, Rb = 94 ppm, Ba = 1082 ppm). Low abundances of compatible and high field strength elements (HFSEs) characterize all studied granitoids, although these elements are, on average, more enriched in tonalites (V = 48 ppm, Cr = 34 ppm, Zr = 155 ppm, Nb = 5.2 ppm) than in granodiorites and monzogranites (V = 17 ppm, Cr = 16 ppm, Zr = 104 ppm, Nb = 4.7 ppm).

Primitive mantle-normalized trace element patterns [109] are fractionated, showing enrichment in incompatible elements by factors of approximately 2 to 300 relative to primitive mantle values. All samples display pronounced negative Nb and Ta anomalies, which are less developed in the latter, as well as marked negative anomalies in P and Ti (Figure 8A,C).

Chondrite-normalized rare earth element (REE) patterns [110] are shown in Figure 8A. Overall, the patterns are steep, with enrichment of light REE (LREE) relative to heavy REE (HREE). Tonalites display La/YbN ratios between 13.5 and 83.4, with negative to positive Eu anomalies (Eu/Eu* = 0.6–1.8) and strong fractionation among both LREE (La/SmN = 3.3–9.5) and HREE (Gd/YbN = 1.9–4.9). Granodiorites and monzogranites exhibit a lower degree of fractionation compared to tonalites, with La/YbN ratios ranging from 6.0 to 45.1, negative to positive Eu anomalies (Eu/Eu* = 0.5–1.5), and moderate fractionation among LREE (La/SmN = 3.2–6.7) and HREE (Gd/YbN = 1.5–4.9) (Figure 8B,D).

5.3. Zircon U-Pb Geochronology and Lu-Hf Isotope Geochemistry

Backscattered electrons (BSEs) imaging on representative zircon grains of the two samples selected for the in situ U-Pb and Lu-Hf analyses are shown in Figure 9. The U−Pb analytical data on zircon are shown in Supplementary Table S3 and plotted on Concordia diagrams (Figure 10). Analyses that showed a high contribution of common Pb (f_{206} values > 0.64%) and discordant analytical points (>20% of discordance in the U-Pb dates) were not used for age calculations. The U-Pb age was calculated using the weighted average of $^{207}Pb/^{206}Pb$ values of the concordant dates, following the recommendations of [111].

The Lu−Hf analytical data on zircon are shown in Supplementary Table S4 and plotted in the $\varepsilon_{Hf(t)}$ versus Age (Ma) diagrams together with existing Hf isotopic data of zircon from rocks of the CP (Figure 11). There is no $^{176}Yb/^{177}Hf$-dependent variation of the $^{176}Hf/^{177}Hf$ ratios that indicates no inappropriate Yb interference affecting the $^{176}Hf/^{177}Hf$ ratios of the zircon following the guidelines of [112–114].

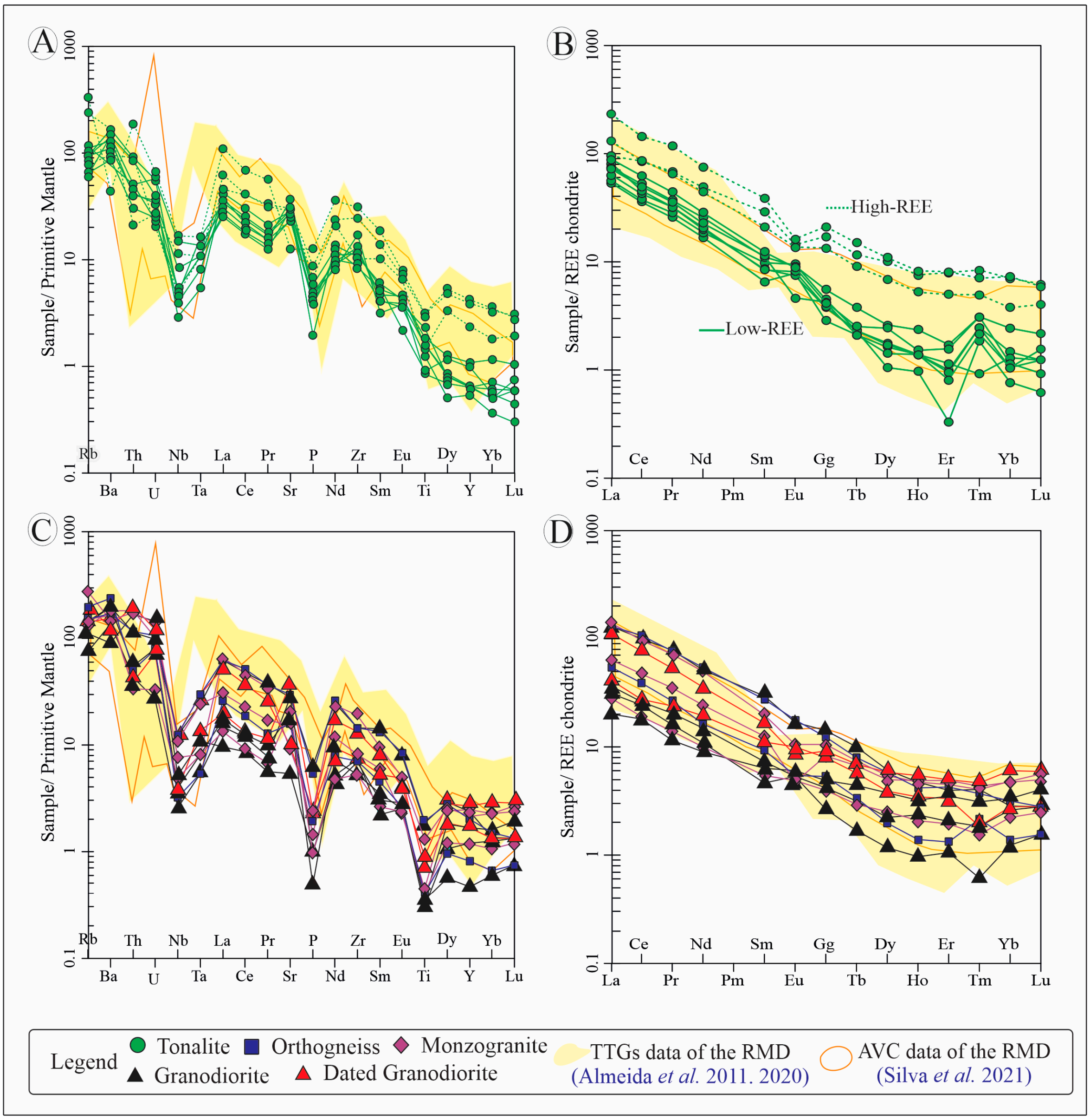

Figure 8. (**A**) Multi-element diagrams for the tonalites (normalized to the primitive mantle of [109]; (**B**) REE distribution patterns for the tonalites (normalized to [110]; (**C**) Multi-element diagrams for granitoids (normalized to the primitive mantle of [109]; and (**D**) REE distribution patterns for granitoids (normalized to [110] for the AVC rocks of the southern part of the Serra do Inajá region. Comparative data references: [30,32,64].

Figure 9. BSE images of zircon crystals of granodiorites from the AVC. Representative illustration displaying the morphology of each crystal, the position of each laser shot, and the corresponding analytical method. (**A**) Sample UP-63; (**B**) Sample RF-130.

5.3.1. Granodiorite Sample UP-63A

Thirty-six spots in zircon grains of the 250–175 µm particle size fraction were analyzed. The crystals are subhedral to anhedral, with preserved edges and some with worn edges, and some crystals show metamictic features. In the BSE images, it can be observed that some crystals show fractures and/or inclusions and incipient zoning in the outer part (Figure 9A—grains H1, I4 and G2, for example). Fifteen crystals, with only one spot per crystal, were used to determine an upper intercept age of 2965 ± 5.7 Ma (MSWD = 1.5). A weighted average $^{207}Pb/^{206}Pb$ age of 2975 ± 7.8 Ma (2σ, MSWD = 0.29) was obtained from six concordant dates (Figure 10A). Lu-Hf isotopic analyses were performed on six concordant and three sub-concordant zircon crystals (80–102% of concordance). The $\varepsilon_{Hf(2.98\ Ga)}$ values are positive between +1.1 and +3.4 with $Hf\text{-}T_{DM}{}^{C}$ model ages of 3.0 to 3.1 Ga. However, two crystals (H4 and I4) yielded negative values of −3.5 and −2.6 with corresponding Hf-$T_{DM}{}^{C}$ model ages of 3.4 Ga (Figure 11).

5.3.2. Granodiorite Sample RF-130

Thirty-six spots in zircon grains from the 250–175 μm granulometric fraction were analyzed. The crystals are predominantly prismatic, subhedral and with worn edges. In the BSE images, the presence of fractures, inclusions and oscillatory magmatic zoning is observed (Figure 9B). The dated zircon population showed a complex age pattern, with three distinct groups of dates. A $^{207}Pb/^{206}Pb$ weighted mean age of 2981 ± 7.0 Ma (2σ, MSWD = 0.89) was obtained for six concordant analyses (Figure 10B). The other three dates were used to determine an upper intercept age of 2851 ± 28 Ma (MSWD = 0.00055, Figure 10B, grains F3, D6 and C5). It is worth noting that the crystals selected for these analytical spots were indistinguishable from those that yielded concordant ages of 2.98 Ga. Another concordant analysis yielded a $^{207}Pb/^{206}Pb$ date of 3055 ± 18 Ma (Figure 9B, grain C4). Lu-Hf isotopic analyses were conducted on six concordant and four sub-concordant zircon crystals (96–98% of concordance), all with a U-Pb age of 2.98 Ga. All $\varepsilon_{Hf(2.98Ga)}$ values were positive and ranged from +0.5 to +3.7. The Hf-$T_{DM}{}^{C}$ model ages varied from 3.0 to 3.2 Ga (Figure 11).

5.4. Whole-Rock Sm-Nd Isotopes

Whole-rock Sm-Nd analyses were performed on the two samples dated by U-Pb on zircon method (granodiorites RF-130 and UP-63A). The results are shown in the ε_{Nd} vs. Age (Ga) diagram (Figure 12) and listed in Supplementary Table S5. $\varepsilon_{Nd(t)}$ values were calculated from the U-Pb crystallization ages here determined for each sample. The granodiorite RF-130 yielded a Nd-T_{DM} model age of 3.0 Ga and a positive $\varepsilon_{Nd(2.98\ Ga)}$ of +2.5. The granodiorite UP-63A provided a Nd-T_{DM} model age of 2.9 Ga and a positive $\varepsilon_{Nd(2.98\ Ga)}$ of +2.9.

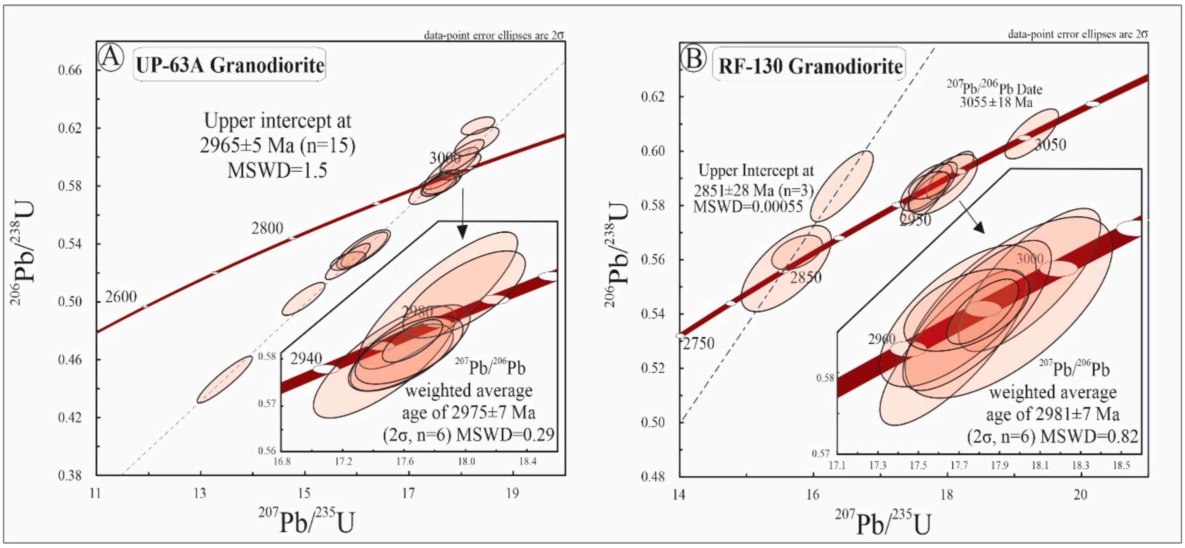

Figure 10. Concordia ($^{206}Pb/^{238}U$ versus $^{207}Pb/^{235}U$) diagrams for U-Pb zircon data obtained for the granodiorites from the AVC. (**A**) Sample UP-63A and (**B**) sample RF-130.

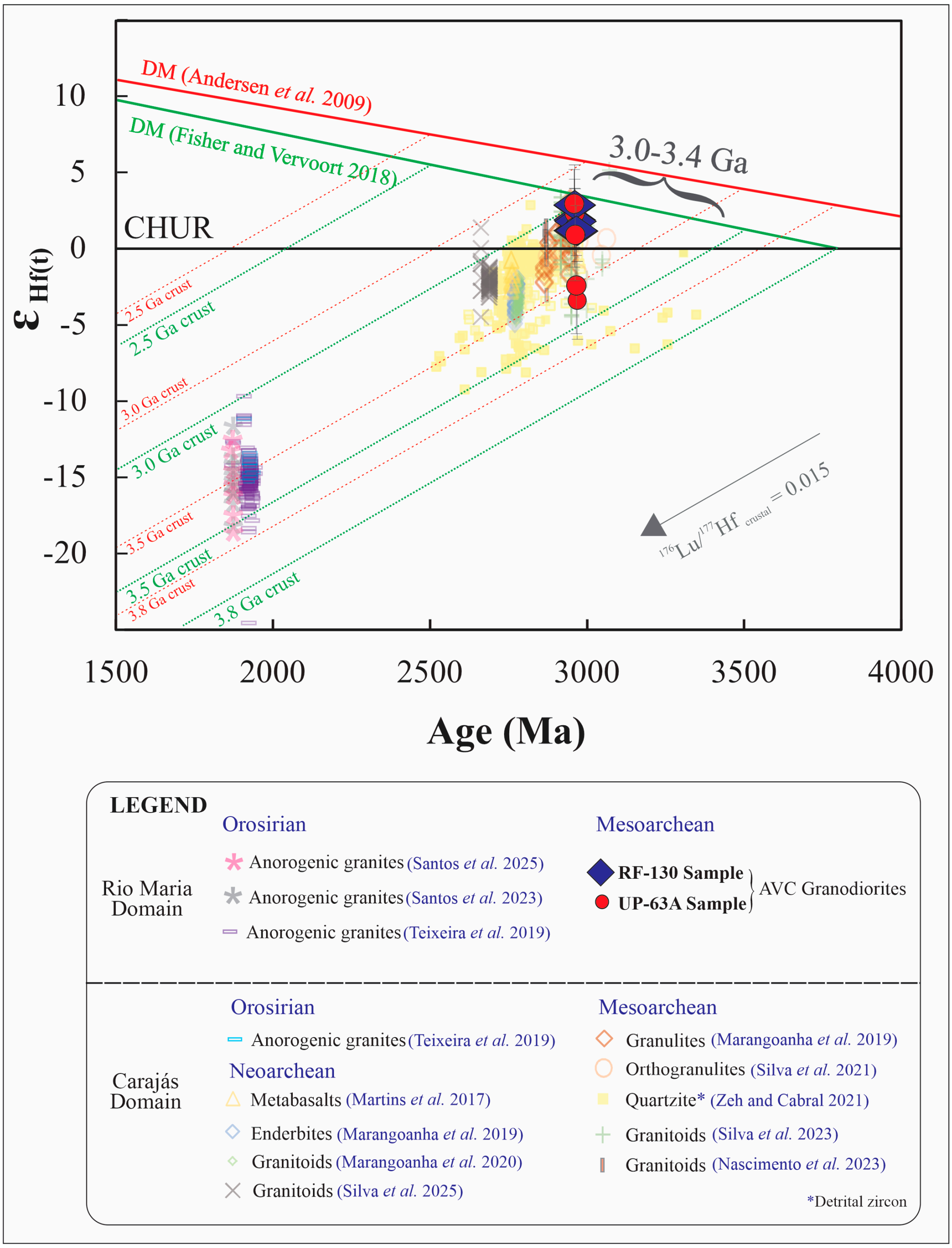

Figure 11. $\varepsilon_{Hf(t)}$ versus age (Ma) diagram for the AVC granitoids from the southern Serra do Inajá region. The dotted lines represent crust evolution trends, calculated using a $^{176}Lu/^{177}Hf$ ratio of 0.015 for an average continental crust [114,115]. Existing Hf isotopic data of zircon crystals from rocks of the CP are displayed in the diagram for comparison. (The data from [37,48,82] are from the RMD and the other data are from the CD). The data used for comparison were recalculated for the 3.8 Ga DM evolution model of [89]. The DM evolution model of [99] is also displayed in the diagram. Geochronological references: [36–40,45,47–49,82,116].

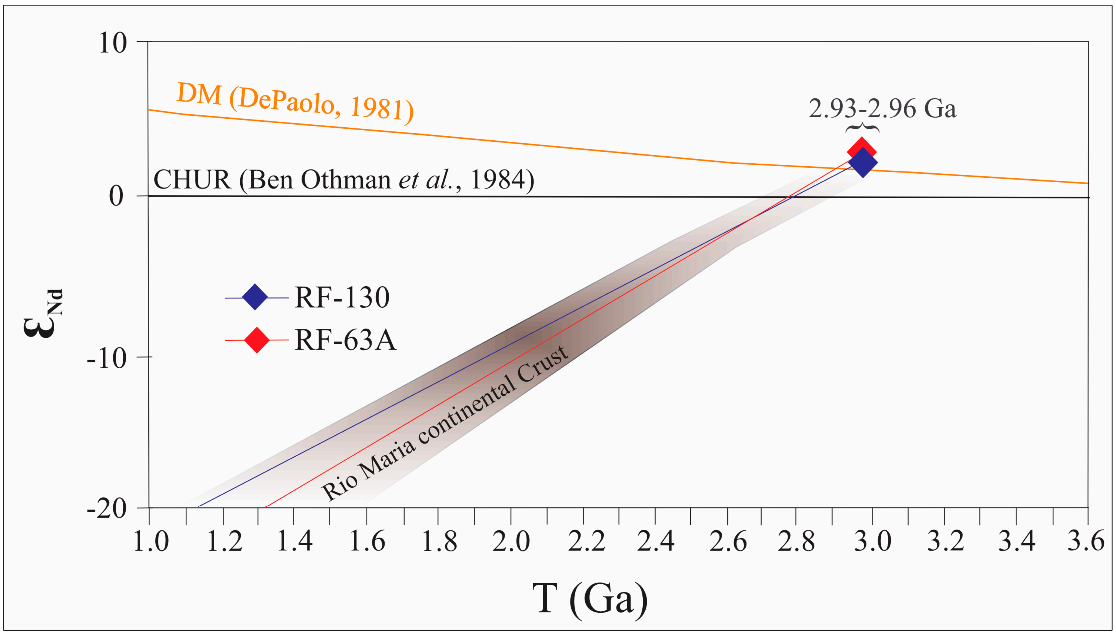

Figure 12. ε_{Nd} vs. age (Ga) diagram for Mesoarchean granitoids from the AVC, southern Serra do Inajá region. The evolution field for the rocks of the RMD [33,42,61,70,91] is presented for comparison. Values for CHUR according to [117] and DM from [118].

6. Discussion

6.1. Age Constraints for the AVC in the Serra do Inajá Region

The zircon U–Pb LA-ICP-MS data obtained for the two analyzed granodioritic samples from the Serra do Inajá region provide robust constraints on the timing of magmatism associated with the AVC. The analytical results show good precision and internal consistency, allowing a confident interpretation of the crystallization ages and a discussion of subordinate age populations.

Sample UP-63A yields a well-defined concordant age of 2975 ± 7 Ma, which is interpreted as the crystallization age of the granodiorite. The dated zircon grains display oscillatory zoning and relatively high Th/U ratios, ranging from 0.44 to 0.90, features that are typical of magmatic zircon. No evidence for inheritance or Pb loss is observed in this sample, reinforcing the interpretation of a single Mesoarchean magmatic event.

Similarly, sample RF-130 yields a concordant age of 2981 ± 7 Ma, which overlaps within analytical uncertainty with the age obtained for UP-63A. Zircon grains from this sample also show well-developed magmatic zoning and Th/U ratios between 0.14 and 1.18, supporting a magmatic origin. The close agreement between the two samples strongly suggests that the ~2.98 Ga age represents the crystallization age of the granodioritic magmatism in the Serra do Inajá area and confirms their affiliation with the AVC.

In sample RF-130, however, two additional concordant age populations were identified, at approximately 2.85 Ga and 3.06 Ga, which require further discussion. An alternative interpretation could consider the ~2.85 Ga age as the crystallization age of the granodiorite, as it overlaps with the emplacement ages of the Rio Maria Granodiorite (2.85–2.89 Ga; ref. [45]). This hypothesis is further supported by the proximity of the sampling site to the mapped limit of the Rio Maria magmatic suite, as defined by [30]. Nevertheless, several lines of evidence argue against this interpretation. The zircon grains yielding ~2.85 Ga ages have distinctly lower Th/U ratios (0.03–0.19) compared to the main 2.98 Ga population, and they do not exhibit significant differences in internal structures or Hf isotopic signatures relative to the older grains, which are remarkably homogeneous. Moreover, the Rio Maria Granodiorite is characterized by a sanukitoid geochemical affinity ([39] and references therein), which contrasts sharply with the geochemical signature of sample RF-130. Taken together, these observations indicate that the ~2.85 Ga ages do not record a primary magmatic crystallization event. Instead, they are best interpreted as reflecting partial reopening of the U–Pb system, likely related to thermal perturbations associated with the emplacement of the nearby Rio Maria batholith.

The older concordant $^{207}Pb/^{206}Pb$ age of ~3.06 Ga identified in RF-130 is interpreted as an inherited component derived from a slightly older crustal source. Although this age has no direct equivalent among the known magmatic events of the RMD, it is comparable to ages reported for the Morada da Prata Formation greenstone belt, dated between 2.96 and 3.07 Ga [30]. Additionally, zircon populations in the range of 3.0–3.08 Ga have been documented as inherited crystals in Mesoarchean granitoids, orthogneisses, and in granulite protoliths of the CD ([47,119] and references therein), suggesting the involvement of older crustal components in the magma source.

Overall, the comparable crystallization ages obtained for samples RF-130 and UP-63A demonstrate that the studied granodiorites belong to a coherent Mesoarchean magmatic episode at ca. 2.98 Ga, which also included coeval tonalites of the AVC dated at 2.98–2.99 Ga by [30,33]. These results confirm that the Serra do Inajá area represents the southernmost extension of the AVC within the RMD. Furthermore, they reinforce the interpretation that the AVC records the oldest recognized magmatic event in the RMD. Importantly, the data show that this early TTG-related magmatism was not restricted to tonalitic and trondhjemitic compositions but also included granitoids of granodioritic affinity. In addition, the ca. 2.98 Ga ages obtained for the AVC granodiorites further demonstrate their contemporaneity with the Serra do Inajá greenstone belt, dated at 2988 ± 4 Ma by [30]. Figure 13 presents a diagram that illustrates, in a simplified way, how the TTGs of the RMD are arranged according to their crystallization ages.

Comparison with available data from the AVC across the RMD suggests that ages from the southern sector (2.98–2.99 Ga; Serra do Inajá region) are slightly older than those from the northern sector (2.94–2.96 Ga) and other sodic granitoid suites (2.91–2.97 Ga). This pattern suggests that AVC magmatism in the Serra do Inajá represents the earliest magmatic episode, broadly coeval with greenstone belt formation, and may reflect an early dome-and-keel (drip tectonics) setting, as proposed by [34,120]. In contrast, younger TTG magmatism from the northern sector is more likely associated with a subduction-related geodynamic context, as suggested by previous studies [32,45,120,121]. Although a gradual transition from stagnant-lid to mobile-lid tectonics appears to be consistent with the RMD during the ~3.0–2.92 Ga interval [120], the available data from the Serra do Inajá region are still limited. Additional geochronological, geochemical, and structural constraints are therefore required to further evaluate the applicability of this model to the southern RMD.

6.2. Petrogenesis of the AVC Mesoarchean Granitoids

6.2.1. Origin of Tonalites

Petrographic and geochemical data indicate that the AVC tonalites correspond to typical TTG suites. These rocks contain biotite and epidote, and rarely amphibole, as the main mafic phases, and plot along the tholeiitic and trondhjemitic trends in the QAP diagram (Figure 4 [122]). They display high SiO_2 contents (average of 68.2 wt%), a sodic character (K_2O/Na_2O = 0.34 on average), and high Al_2O_3 contents (average of 15.5 wt%), comparable to the high-Al_2O_3 TTG described by Barker [105]. The tonalites show moderate Mg# values (~0.39), placing them within the field of magnesian granitoids [106]. The sum of ferromagnesian oxides is typically below 10.4 wt%, with an average of 5.5 wt%. Overall, the samples plot near alumina saturation (A/CNK ≈ 1.0, Figure 6E), and CIPW-normative corundum contents are below 1.0%.

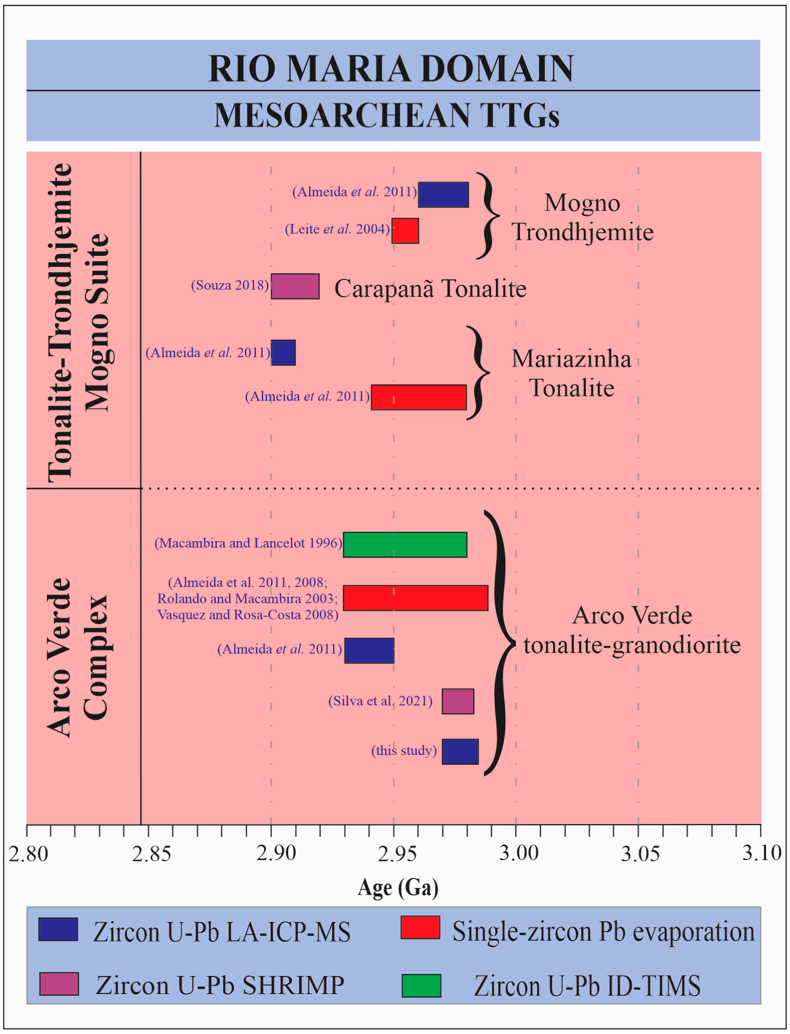

Figure 13. Zircon U-Pb and Pb-Pb age compilation of TTG rocks from the RMD (Rio Maria Domain). LA–ICP–MS = laser ablation inductively coupled plasma mass spectrometry; SHRIMP = sensitive high-resolution ion microprobe; and ID-TIMS = isotope dilution thermal ionization mass spectrometry. References: [29–33,68,85,92].

The high SiO_2 contents, coupled with low Mg# values and low concentrations of compatible elements (e.g., Cr, V, and Ni), suggest a dominantly crustal origin for the tonalites. These features are consistent with experimental melts derived from metabasalts and eclogites [123], with no clear evidence for direct mantle involvement. In the Al_2O_3/(FeO* + MgO)–(3CaO)–($5K_2O/Na_2O$) ternary diagram (Figure 14A [4]), the samples plot mainly within the field of melts derived from low-K mafic rocks, indicating a predominantly mafic crustal source.

Despite similar major-element compositions, the tonalites exhibit marked variability in REE contents and can be subdivided into low- and high-HREE groups (Figure 8B). The low-HREE tonalites, which represent most of the samples, are characterized by low Y (2.3–4.6 ppm) and Yb (0.16–0.51 ppm) contents, variable Eu anomalies (Eu/Eu* = 0.7–1.8), and strongly fractionated REE patterns (La_N/Yb_N = 30.4–83.4). In contrast, the high-HREE tonalites display higher Y (10.1–17.9 ppm) and Yb (0.79–1.53 ppm) contents, systematic negative Eu anomalies (Eu/Eu* = 0.6–0.8), and moderately fractionated REE patterns (La_N/Yb_N = 13.5–34.5; Figure 15A). Strontium contents are high and similar in both groups (average of 537 ppm), resulting in low Sr/Y ratios for the high-HREE tonalites (36.3–56.2) and high Sr/Y ratios for the low-HREE tonalites (170–221). These features are comparable to those of adakites from modern island arcs (Figure 14B [13,124]).

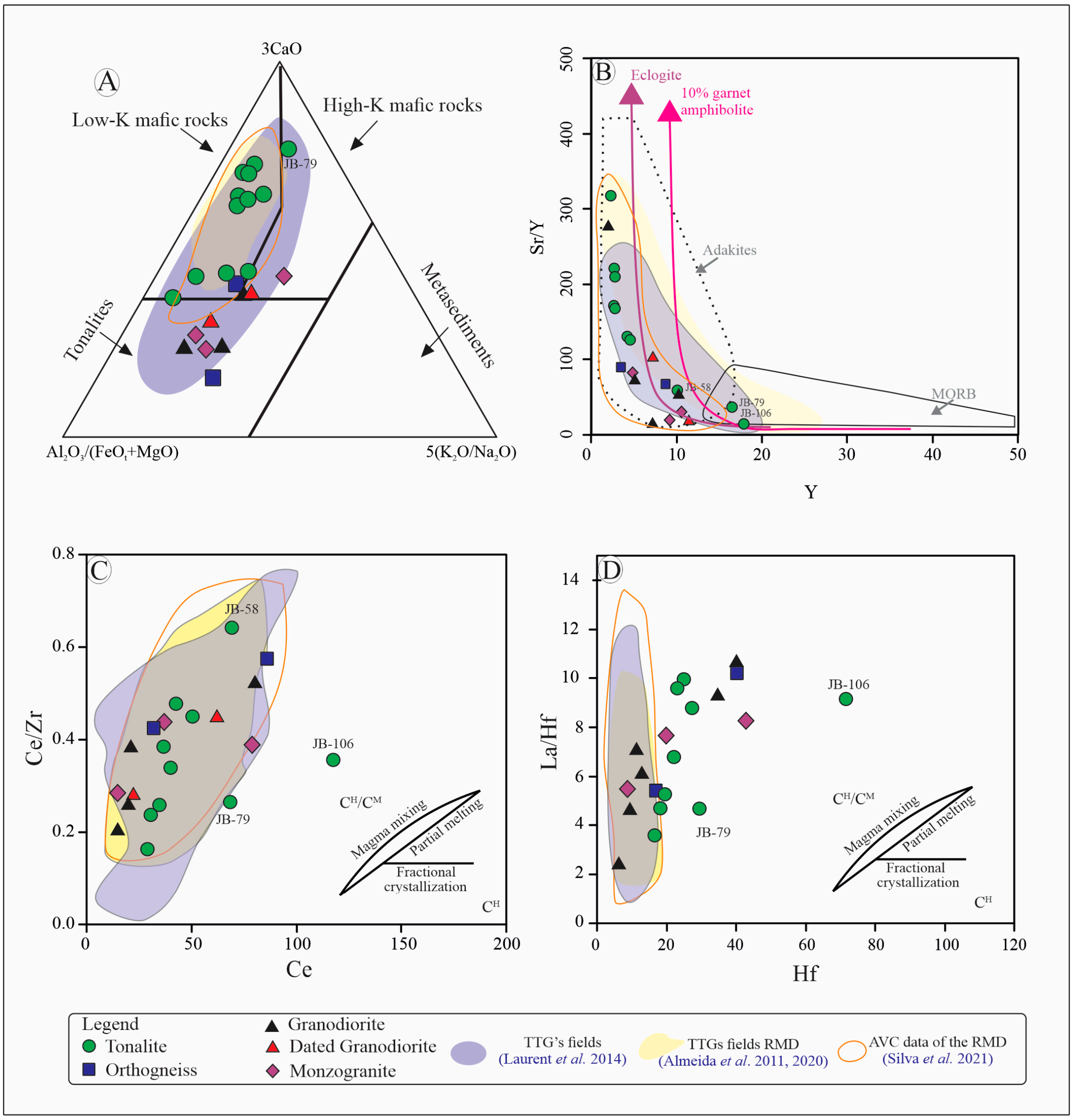

Figure 14. (**A**) $Al_2O_3/(FeOt + MgO)$–3.CaO–5.(K_2O/Na_2O) diagram. The fields represent the composition of magmas from various sources (tonalites, metasediments, low and high K mafic rocks [4]; (**B**) Discriminant diagram for TTGs and adakitic rocks (Sr/Y vs. Y plot) from [124]; (**C**) Ce/Zr versus Ce magmatic differentiation diagram; (**D**) La/Hf versus Hf tectonic discrimination diagram. Comparative data references: [4,30,32,64].

Compositional variability within TTG suites is commonly attributed to either fractional crystallization or partial melting at different depths [13,125,126]. In Ce versus Ce/Zr and Hf vs. La/Hf diagrams (Figure 14C,D), the tonalite samples define positive correlations, indicating that partial melting was the dominant petrogenetic process, rather than fractional crystallization [127]. Accordingly, the observed compositional variability of the AVC tonalites is best explained by differences in melting depth.

Based on melting depth and corresponding residual mineral assemblages, TTG can be classified into: (i) low-pressure types, characterized by plagioclase-rich residues; (ii) medium-pressure types, with residues dominated by garnet and amphibole; and (iii) high-pressure types, derived from rutile-bearing eclogitic assemblages [13,125,126]. The low-HREE tonalites characterized by high Sr/Y and La_N/Yb_N ratios, low Nb-Ta contents, and predominantly positive Eu anomalies are consistent with melts equilibrated with residues containing abundant garnet and minor rutile, but minor or no plagioclase (Figure 15A,C).

Conversely, the high-HREE tonalites are characterized by lower Sr/Y ratios, moderate La_N/Yb_N values (Figures 14B and 15B), and weak negative Eu anomalies (Figure 14C), indicating the presence of plagioclase in the melting residue. Their low Nb-Ta contents further suggest the involvement of accessory Ti-bearing phases, such as titanite or ilmenite. Together, these data indicate that both tonalite groups originated from partial melting of a similar mafic source at different crustal depths: high-HREE tonalites formed at shallower crustal levels where plagioclase was stable, whereas low-HREE tonalites formed at greater depths under high-pressure conditions where garnet and rutile were stable. This interpretation is supported by the low-HREE tonalites plotting within the garnet-bearing source field in the 1/Er–(Ba + Sr)/1000–Er ternary diagram (Figure 15C [128]), whereas two high-HREE tonalite samples fall outside this field. These results are consistent with previous data reported by [30] for TTG samples from the AVC, which also identified both high- and low-pressure TTGs in the AVC.

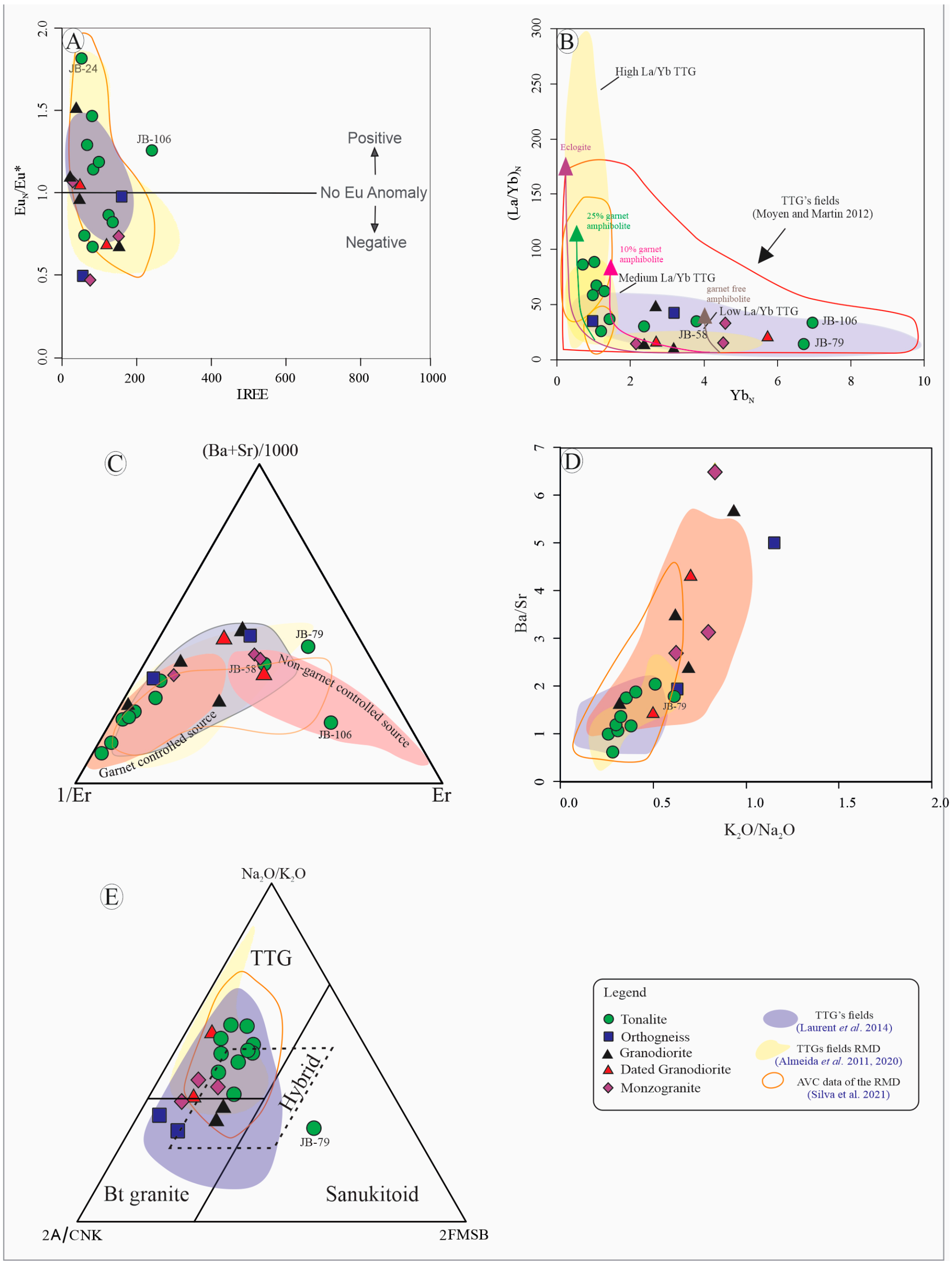

Figure 15. (**A**) EuN/Eu* vs. LREE diagram (EuN = Eu concentration normalized to C1 chondrites; ref. [109]) (**B**) *(La/Yn)N* vs. *YbN for Archean TTGs* [129]; (**C**) Discriminant diagram of garnet-controlled

(pole 1/Er) and nongarnet-controlled (pole Er) sources. The third pole (Ba + Sr)/1000 represents an enriched mantle source [128]; (**D**) *Ba/Sr* vs. *K_2O/Na_2O diagram* [125]; and (**E**) ternary classification diagram for late Archean granitoids: 2.A/CNK (=2.$[Al_2O_3/(CaO + Na_2O + K_2O)]_{mol}$); Na_2O/K_2O; FMSB (=2.$(FeOt + MgO)_{wt\%}$.$(Sr + Ba)_{wt\%}$ [4]). *Comparative data references*: [4,30,32,64].

6.2.2. Origin of Granodiorites and Granites

Granodiorites and granites differ markedly from tonalites in both major- and trace-element compositions. They display higher SiO_2 contents (average of 74.3 wt%), lower Mg# values (average of 0.21), lower ferromagnesian oxide sums (<4.0 wt%), and higher K_2O contents, resulting in higher K_2O/Na_2O ratios (average of 0.66) compared to tonalites. Only sample UP-70A shows a distinctly potassic character ($K_2O/Na_2O > 1$), likely reflecting the presence of minor K-feldspar derived from anatectic melts; this sample is therefore treated separately.

All samples are slightly peraluminous, A/CNK values (A/CNK ≈ 1.0; Figure 6E), and plot within the field of ferroan granitoids [90,106]. In the normative Ab–Or–An diagram, they fall within the trondhjemite, granodiorite, and granite fields [105]. On Na–K–Ca plots, these rocks define an intermediate trend between the calc-alkaline and trondhjemitic evolutionary paths, reflecting their transitional character [11,12].

LILE contents are significantly higher than in the tonalites (Ba ≈ 1082 ppm; Rb ≈ 94 ppm), whereas Sr is lower (average 393 ppm). Y contents overlap those of the tonalites, leading to a wide range of Sr/Y ratios (15–277).

In a K_2O/Na_2O vs. Ba/Sr plot (Figure 15D), the samples overlap the Rio Maria leucogranodiorite–granite suite [130] and transitional TTGs from the Yilgarn Craton [131]. In the 2A/CNK–Na_2O/K_2O–2FMSB ternary diagram (Figure 15E [4]), the span the compositional fields of TTG and biotite granitoids and overlap the domain of hybrid granitoids.

The low Mg# values and low concentrations of compatible elements (V ≈ 16.5 ppm and Cr ≈ 15.5 ppm on average), combined with higher K contents, indicate a more evolved source than that of the tonalites. This is supported by the Al_2O_3/(FeO* + MgO)–(3CaO)–($5K_2O/Na_2O$) ternary diagram (Figure 14A [4]), where the samples plot near melts derived from tonalitic and high-K mafic sources, similar to the RMD leucogranodiorite-granite suite [130]. These geochemical characteristics imply the involvement of preexisting felsic continental crust and an enriched source component, possibly of mantle affinity.

However, a purely tonalitic source does not account for the trace-element signatures. The general absence of pronounced negative Eu and Sr anomalies in multi-element diagrams argues against significant plagioclase retention in the residue, as would be expected during tonalitic crustal melting (Figure 8D). Instead the moderately fractionated REE patterns require the presence of a phase preferentially retaining HREE, such as garnet. The involvement of amphibole and garnet in the source region is further supported by Sr/Y vs. Y (Figure 14B) and La_N/Yb_N vs. Yb (Figure 15A) relationships [13,124]. Additionally, strong negative Nb, Ta, and Ti anomalies indicate retention by Ti-bearing phases, while preferential Nb depletion relative to Ta suggests rutile and/or ilmenite as the dominant controlling accessory phases [132].

Experimental studies have demonstrated that voluminous granodioritic magmas can form through interaction between hydrous, mantle-derived mafic magmas and felsic tonalitic crust [133]. In this model, water released from hydrous, LILE-enriched mafic magmas lowers the solidus of the surrounding felsic crust, promoting granodioritic melt generation. An alternative model proposed by [32,121] for the Rio Maria leucogranodiorite-granite suite invokes the transfer of LILE-rich fluids derived from sanukitoid magmas into TTG crust, supplying both H_2O and incompatible elements. Regardless of the specific mechanism, the recognition of transitional TTGs in the AVC indicates the presence of both felsic and mafic crust that was rapidly reworked shortly after its formation during the Mesoarchean.

https://doi.org/10.3390/min16050483

6.2.3. Integrated Petrogenetic Model and Regional Tectonic Implications

The coeval occurrence of tonalites and granodiorites/granites indicates that multiple processes operated simultaneously: (i) partial melting of metabasalt at variable depths, producing low-HREE (high-pressure, garnet ± rutile) and high-HREE (low-pressure, plagioclase) tonalites; (ii) mantle–crust interaction, with hydrated mafic magmas inducing melting of tonalitic crust and LILE enrichment; and (iii) fluid transfer, supplying H_2O and incompatible elements to the TTG crust and generating leucogranodiorites and granites [32,64,93,120,130,134,135].

This model explains the magmatic diversity and indicates that the AVC records both deep crustal melting and interaction with mantle-derived magmas, pointing to a complex, multi-stage Mesoarchean crustal evolution.

The diversity of coeval magmas suggests that the Carajás Province developed under complex Mesoarchean tectonic conditions, where plume-related vertical processes may have coexisted with incipient subduction [34,39,45,120]. Tonalites reflect melting of mafic crust at variable depths, whereas granodiorites/granites record hybridization and crustal reworking.

This interpretation is consistent with models proposing a transition from stagnant-lid to mobile tectonics, involving both vertical processes and early subduction [4,13,23]. Similar TTG–potassic granitoid associations in other Archean cratons (Barberton, [136]; Pilbara, [137]; Yilgarn, [137]; Karelia) indicate that Mesoarchean crustal evolution was widely controlled by coeval processes. In the AVC, this diversity reflects rapid crustal reorganization with implications for early continental crust formation

6.3. Crustal Growth in the Carajás Province

The combined U–Pb–Lu–Hf zircon and whole-rock Sm–Nd isotopic dataset obtained for the oldest magmatic rocks of the CP provides a robust framework for investigating Mesoarchean continental crust generation. Notably, these data include the first Lu–Hf isotopic results for the Mesoarchean basement of the RMD, enabling integration with existing isotopic constraints from the CD and contributing to a more comprehensive understanding of the CP. The integration of zircon Hf and whole-rock Nd systems provides strong constraints on magma sources and crustal evolution, reducing ambiguities inherent to single-isotope approaches.

The Sm–Nd isotopic data for both samples yield Nd–T_{DM} model ages of 2.9–3.0 Ga and positive $\varepsilon_{Nd(t)}$ values (+2.9 and +2.5), consistent with a depleted mantle signature. These results indicate that the Mesoarchean magmatism in the Serra do Inajá region originated predominantly from mantle-derived sources, with negligible contribution from older crustal components.

Zircons from the granodiorite sample RF-130 yield exclusively suprachondritic $\varepsilon_{Hf(t)}$ values (+0.5 to +3.7) and Hf-$T_{DM}{}^{C}$ model ages between 3.0 and 3.2 Ga, close to the crystallization age of ca. 2.98 Ga. These features are consistent with derivation from juvenile sources and suggest magma generation from recently extracted mantle-derived crust. Similarly, zircons from the granodiorite sample UP-63A display predominantly suprachondritic $\varepsilon_{Hf(t)}$ values (+1.1 to +3.4) and comparable model ages (Hf-$T_{DM}{}^{C} \approx$ 3.0–3.1 Ga), pointing to a dominantly juvenile crustal source. However, two zircon grains from this sample yield negative $\varepsilon_{Hf(t)}$ values (−3.5 and −2.6) associated with slightly older Hf model ages around 3.4 Ga, indicating minor input of an older crustal component.

The concordance between the Sm–Nd and Lu–Hf model ages, both pointing to a juvenile origin, supports the hypothesis that the geological evolution of the Serra do Inajá region was marked by primitive magmatic pulses around 3.0–3.2 Ga, which played an important role in the initial construction of the crust within the Rio Maria Domain.

https://doi.org/10.3390/min16050483

A comparison of compiled Nd–T_{DM} model ages for the Archean magmatic rocks of the CD and RMD domains reveals a common age peak at ca. 3.05 Ga (Figure 16A), supporting the interpretation that the continental crust of the Carajás Province formed during a single Mesoarchean magmatic episode. Hf isotopic data from Archean magmatic rocks of both domains similarly define age peaks at ~3.1 Ga (Figure 16B), further indicating significant crustal generation during Mesoarchean in the CP, with no clear distinction between northern and southern sectors. These observations suggest that the province represents a coherent crustal block formed during a major Mesoarchean crustal growth event, in agreement with [120].

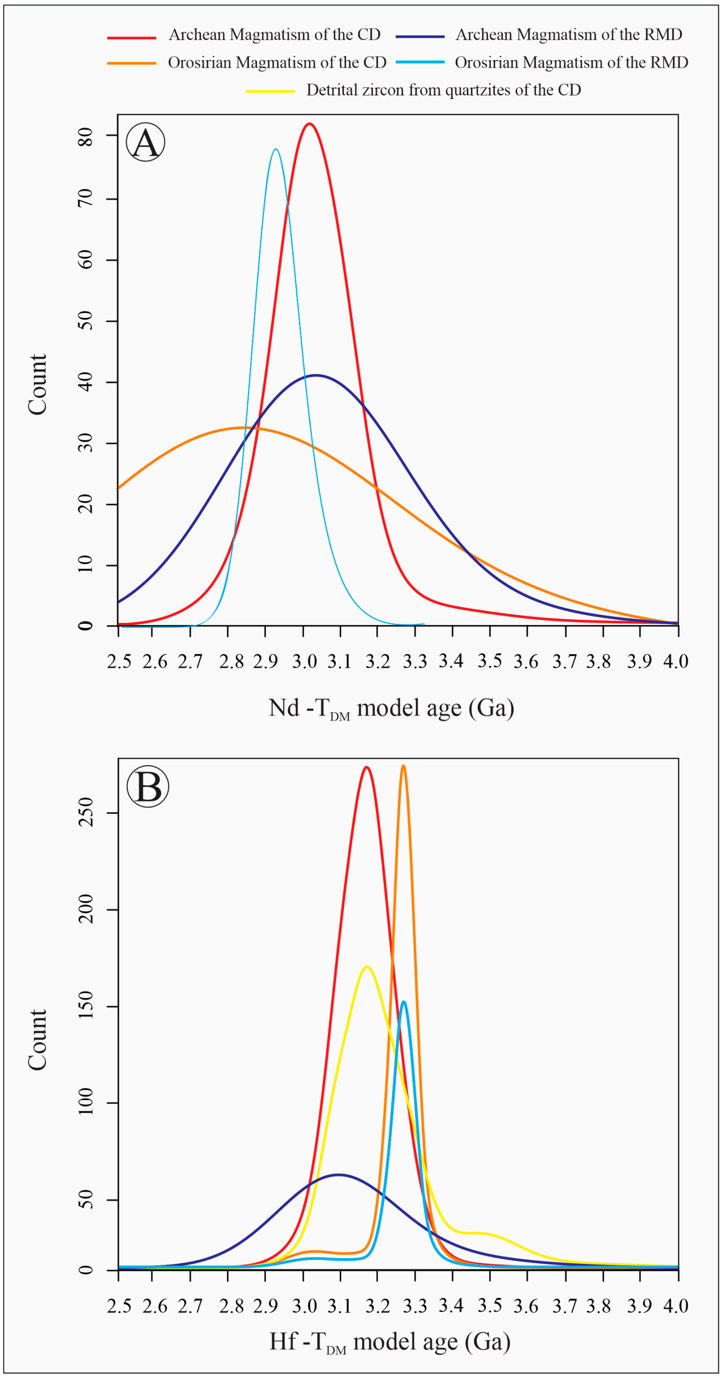

Figure 16. Frequency histograms showing the depleted mantle ages (T_{DM}) obtained for the Archean rocks of the CD and RMD, from the CP. In (**A**), the Nd-T_{DM} ages [33,35,42,46,61,70,76,91,94,138,139], and in (**B**), the Hf-$T_{DM}{}^{C}$ ages [36–40,45,47–49,116].

The adoption of a depleted mantle Hf evolution model initiated at ca. 3.8 Ga [89] (see discussion below) allows reconciliation of the Hf and Nd isotopic datasets by reducing discrepancies between model ages derived from the two systems, further supporting predominantly juvenile crust formation during this stage of the Carajás Province evolution (Figure 16A).

6.4. Differentiation of the Depleted Mantle Beneath the Carajás Province

Hafnium crustal model ages (Hf–$T_{DM}{}^{C}$) reported for magmatic rocks from the CP and, more broadly, the Amazonian Craton have commonly been calculated using the classical depleted mantle (DM) model of [119] and references therein. In this approach, the isotopic composition of the DM is assumed to be represented by average mid-ocean ridge basalt (MORB), with $^{176}Lu/^{177}Hf$ = 0.0388 and $^{176}Hf/^{177}Hf$ = 0.283250, and mantle differentiation is assumed to start at 4.56 Ga. Application of this model has yielded very old Hf model ages, reaching up to ca. 4.0 Ga for magmatic rocks and detrital zircons from the Amazonian Craton.

However, the timing of the establishment of a depleted mantle reservoir for Hf isotopes has been widely debated over the past decade (e.g., refs. [89,140–142] and references therein), and alternative evolutionary models have been proposed. Based on a global compilation of zircon Hf isotope data, ref. [89] argued that there is no compelling evidence for early Hadean mantle depletion. The near-complete destruction of Hadean continental crust, combined with the scarcity of Eoarchean zircons with suprachondritic ε_{Hf} values, suggests that a globally depleted mantle reservoir did not exist prior to ca. 3.8 Ga. Mulder et al. [143] suggested a major shift in global mantle–crust geodynamics during the Hadean–Eoarchean transition when the stabilization of a depleted mantle enabled the crustal rejuvenation and formation of stable evolved crust. More recently, Ref. [142] emphasized the strong heterogeneity of Hf isotopic signatures among Archean–Proterozoic terranes and proposed that regionally defined mantle reference curves are more appropriate.

For the Carajás Province, we adopt the model of [89], which assumes that mantle depletion began at ca. 3.8 Ga. Constraining the onset of mantle depletion beneath the province would require isotopic and geochronological data from Paleo- to Eoarchean rocks (i.e., U–Pb zircon ages up to ~3.8 Ga), which are not currently recognized. The oldest magmatic event identified in the province is early Mesoarchean (~3.0 Ga). Initiating mantle depletion at this age would be inconsistent with the Hf isotope data, as suprachondritic ε_{Hf} values from Mesoarchean rocks would plot above the corresponding DM evolution line. In contrast, assuming an onset at ca. 3.8 Ga yields a DM trajectory compatible with the Hf isotope composition of most magmatic rocks from the province (Figure 16). Only a single xenocrystic zircon from a Mesoarchean sanukitoid plots above the DM curve [45].

Using a mantle differentiation age of ca. 3.8 Ga also affects model age calculations. Under this assumption, Hf–$T_{DM}{}^{C}$ model ages are systematically younger by ~150 Myr, yielding values between ca. 3.0 and 3.4 Ga. These revised ages show improved agreement with Nd–T_{DM} model ages (ca. 3.0–3.2 Ga), supporting the internal consistency of the adopted mantle evolution model and reinforcing the interpretation of Mesoarchean crustal growth in the province (Figure 16A).

Additionally, indirect evidence supports the possible existence of Eoarchean crust beneath or adjacent to the CP. Orosirian granites commonly yield slightly older Hf–$T_{DM}{}^{C}$ model ages than the exposed Archean basement (Figure 16B), suggesting the involvement of an older crustal component. In contrast, Nd–T_{DM} model ages cluster around 2.9 Ga in Orosirian granites of both the CD and RMD, suggesting a contribution from juvenile material alongside a dominant Mesoarchean crustal source. However, some of these granites record older whole-rock Nd–T_{DM} ages of 3.3–3.4 Ga in the CD Figure 16A; refs. [51,144], pointing to older, unexposed crustal remnants.

Detrital zircons from quartzites of the Carajás and Rio Maria domains yield U–Pb ages between 3.4 and 3.7 Ga [49,73], and an inherited zircon age of 3.68 Ga has been reported from gneisses in the westernmost sector [145]. Moreover, detrital zircons yield Hf–$T_{DM}{}^{C}$ model ages up to 3.85–3.90 Ga [49], consistent with a mantle depletion onset at ca. 3.8 Ga (Figures 11 and 16B).

The predominance of chondritic to suprachondritic Hf isotopic signatures in Mesoarchean zircons, together with sub-chondritic signatures in detrital zircons, provides further evidence for juvenile magmatic sources with minor contributions from older crust. These observations, combined with a mantle depletion onset at ca. 3.8 Ga, are consistent with the models proposed by [89,142,143]. Although additional Lu–Hf data from Archean rocks of the RMD are required to further test this interpretation, these models currently provide a coherent framework for interpreting Hf isotope systematics and crust–mantle evolution in the CP.

7. Conclusions

The integrated petrographic, geochemical, U–Pb zircon geochronological, and Nd–Hf isotopic study of granitoids from the AVC in the Serra do Inajá region establishes important constraints on the crustal evolution of the southern sector of the RMD.

The AVC is dominantly composed of tonalites, with subordinate granodiorites and monzogranites. Crystallization ages of 2979 ± 8 Ma and 2979 ± 11 Ma obtained for two granodiorites, together with the previously published ages of ca. 2.98 Ga for tonalites, suggest that TTG magmatism in the southern RMD is broadly contemporaneous with that of the northern sector. This confirms the regional extent of the Mesoarchean magmatic event and consolidates the AVC as one of the oldest and most extensive granitoid units of the RMD.

Geochemical characteristics indicate that the tonalites correspond to typical TTGs generated by partial melting of a compositionally similar mafic source at different crustal depths. In contrast, the granodiorites and monzogranites display affinities with transitional TTGs, indicating the coexistence of felsic and mafic crust in the AVC during the Mesoarchean. Both crustal components were rapidly reworked shortly after their formation.

Hf and Nd model ages between 3.0 and 3.2 Ga, combined with positive ε_{Hf} and ε_{Nd} values at 2.98 Ga, are further evidence that the main period of crustal extraction and growth in the Carajás Province occurred during the Early Mesoarchean.

Based on the available Hf isotopic dataset for the Carajás Province, we further propose that the differentiation of the depleted mantle (DM) beneath the province may have initiated around 3.8 Ga. Although this interpretation is supported by the current dataset, additional Lu–Hf isotopic data from Archean rocks of the Rio Maria Domain are required to validate this interpretation.

Supplementary Materials: The following supporting information can be downloaded at: https://www.mdpi.com/article/10.3390/min16050483/s1, Table S1: Petrographic data of Mesoarchean Granitoids from the Arco Verde Complex; Table S2: Geochemical data of Mesoarchean Granitoids from the Arco Verde Complex; Table S3: U-Pb zircon data of Mesoarchean Granitoids from the Arco Verde Complex; Table S4: Lu-Hf in zircon data of Mesoarchean Granitoids from the Arco Verde Complex; Table S5: Sm-Nd in whole rock of Mesoarchean Granitoids from the Arco Verde Complex; Supplementary_Material_Analytical_Procedures [144,146–165].

Author Contributions: Methodology, J.-M.L., J.M.M.N., F.d.S.P. and E.L.D.; Software, J.M.M.N. and F.d.S.P.; Validation, J.-M.L.; Formal analysis, B.K.C.N.; Resources, J.-M.L., R.C.d.S.S. and E.L.D.;

Writing—original draft, B.K.C.N.; Writing—review and editing, B.K.C.N., J.-M.L., J.M.M.N. and F.d.S.P.; Supervision, J.-M.L. and R.C.d.S.S. All authors have read and agreed to the published version of the manuscript.

Funding: This research was funded by the Coordenação de Aperfeiçoamento de Pessoal de Nível Superior (CAPES; grant no. 88882.347892/2019-01 to B.K.C. Nogueira) and the Conselho Nacional de Desenvolvimento Científico e Tecnológico (CNPq; grant no. 308747/2025-9 to J.M. Lafon). Additional funding was provided by the PRONEX/FAPESPA/CNPq project no. 062/2020).

Data Availability Statement: Data are available in this article and its Supplementary Materials.

Acknowledgments: The authors thank the Isotope Geology Laboratory (Pará-Iso), the Postgraduate Program in Geology and Geochemistry (PPGG), and the Microanalysis and Thin Section Laboratories of the Institute of Geosciences at UFPA, as well as the Laboratory of Geodynamics, Geochronology and Environmental Studies (LEGGA/UnB), for their technical support. The authors are especially grateful to the Geological Survey of Brazil (Belém unit) for providing samples and geological data from the Geological–Geophysical–Metallogenic Integration Project of the Rio Maria Domain greenstone belt sequences. The authors also thank Cláudio Lamarão, José Arimateia Almeida, and Moacir Macambira for valuable discussions and assistance. The authors are also grateful to four anonymous reviewers for their valuable comments and suggestions, which significantly improved the quality of this manuscript.

Conflicts of Interest: The authors declare no conflicts of interest.

References

1. Moyen, J.-F.; Laurent, O. Archaean Tectonic Systems: A View from Igneous Rocks. *Lithos* **2018**, *302–303*, 99–125. [CrossRef]
2. Taylor, S.R.; McLennan, S.M. *The Continental Crust: Its Composition and Evolution. An Examination of the Geochemical Record Preserved in Sedimentary Rocks*; Blackwell Scientific: Oxford, 1985.
3. Condie, K.C.; Aster, R.C. Episodic Zircon Age Spectra of Orogenic Granitoids: The Supercontinent Connection and Continental Growth. *Precambrian Res.* **2010**, *180*, 227–236. [CrossRef]
4. Laurent, O.; Martin, H.; Moyen, J.F.; Doucelance, R. The Diversity and Evolution of Late-Archean Granitoids: Evidence for the Onset of "Modern-Style" Plate Tectonics between 3.0 and 2.5 Ga. *Lithos* **2014**, *205*, 208–235. [CrossRef]
5. Condie, K.C.; O'Neill, C.; Aster, R.C. Evidence and Implications for a Widespread Magmatic Shutdown for 250 My on Earth. *Earth Planet. Sci. Lett.* **2009**, *282*, 294–298. [CrossRef]
6. Simon, M.B.; Bongiolo, E.M.; Ávila, C.A.; Teixeira, W.; Marimon, R.S.; Oliveira, E.P. Archean Sodic Metagranitoids from the Southern São Francisco Craton: Review, Petrogenesis, and Tectonic Implications. *Lithos* **2021**, *398–399*, 106246. [CrossRef]
7. Taylor, S.R.; McLennan, S.M. The Geochemical Evolution of the Continental Crust. *Rev. Geophys.* **1995**, *33*, 241–265. [CrossRef]
8. Kramers, J.D.; Tolstikhin, I.N. Two Terrestrial Lead Isotope Paradoxes, Forward Transport Modelling, Core Formation and the History of the Continental Crust. *Chem. Geol.* **1997**, *139*, 75–110. [CrossRef]
9. Belousova, E.A.; Kostitsyn, Y.A.; Griffin, W.L.; Begg, G.C.; O'Reilly, S.Y.; Pearson, N.J. The Growth of the Continental Crust: Constraints from Zircon Hf-Isotope Data. *Lithos* **2010**, *119*, 457–466. [CrossRef]
10. Dhuime, B.; Hawkesworth, C.; Cawood, P. When Continents Formed. *Science* **2011**, *331*, 154–155. [CrossRef]
11. Barker, F.; Arth, J.G. Generation of Trondhjemitic-Tonalitic Liquids and Archean Bimodal Trondhjemite-Basalt Suites. *Geol* **1976**, *4*, 596. [CrossRef]
12. Martin, H. Chapter 6 The Archean Grey Gneisses and the Genesis of Continental Crust. In *Developments in Precambrian Geology*; Elsevier: Amsterdam, The Netherlands, 1994; pp. 205–259. ISBN 978-0-444-81621-4.
13. Moyen, J.-F.; Martin, H. Forty Years of TTG Research. *Lithos* **2012**, *148*, 312–336. [CrossRef]
14. Stern, R.J. Evidence from Ophiolites, Blueschists, and Ultrahigh-Pressure Metamorphic Terranes That the Modern Episode of Subduction Tectonics Began in Neoproterozoic Time. *Geol* **2005**, *33*, 557. [CrossRef]
15. Hopkins, M.; Harrison, T.M.; Manning, C.E. Low Heat Flow Inferred from >4 Gyr Zircons Suggests Hadean Plate Boundary Interactions. *Nature* **2008**, *456*, 493–496. [CrossRef] [PubMed]
16. Cawood, P.A.; Kröner, A.; Pisarevsky, S. Precambrian Plate Tectonics: Criteria and Evidence. *Gsa Today* **2006**, *16*, 4. [CrossRef]
17. Smithies, R.H.; Van Kranendonk, M.J.; Champion, D.C. The Mesoarchean Emergence of Modern-Style Subduction. *Gondwana Res.* **2007**, *11*, 50–68. [CrossRef]

18. Van Kranendonk, M.J.; Hugh Smithies, R.; Hickman, A.H.; Champion, D.C. Review: Secular Tectonic Evolution of Archean Continental Crust: Interplay between Horizontal and Vertical Processes in the Formation of the Pilbara Craton, Australia. *Terra Nova* **2007**, *19*, 1–38. [CrossRef]
19. Sizova, E.; Gerya, T.; Brown, M.; Perchuk, L.L. Subduction Styles in the Precambrian: Insight from Numerical Experiments. *Lithos* **2010**, *116*, 209–229. [CrossRef]
20. Hamilton, W.B. Plate Tectonics Began in Neoproterozoic Time, and Plumes from Deep Mantle Have Never Operated. *Lithos* **2011**, *123*, 1–20. [CrossRef]
21. Bédard, J.H. Stagnant Lids and Mantle Overturns: Implications for Archaean Tectonics, Magmagenesis, Crustal Growth, Mantle Evolution, and the Start of Plate Tectonics. *Geosci. Front.* **2018**, *9*, 19–49. [CrossRef]
22. Nebel, O.; Capitanio, F.A.; Moyen, J.-F.; Weinberg, R.F.; Clos, F.; Nebel-Jacobsen, Y.J.; Cawood, P.A. When Crust Comes of Age: On the Chemical Evolution of Archaean, Felsic Continental Crust by Crustal Drip Tectonics. *Phil. Trans. R. Soc. A.* **2018**, *376*, 20180103. [CrossRef]
23. Condie, K.C. A Planet in Transition: The Onset of Plate Tectonics on Earth between 3 and 2 Ga? *Geosci. Front.* **2018**, *9*, 51–60. [CrossRef]
24. Hawkesworth, C.; Cawood, P.A.; Dhuime, B. Rates of Generation and Growth of the Continental Crust. *Geosci. Front.* **2019**, *10*, 165–173. [CrossRef]
25. Brown, M.; Johnson, T.; Gardiner, N.J. Plate Tectonics and the Archean Earth. *Annu. Rev. Earth Planet. Sci.* **2020**, *48*, 291–320. [CrossRef]
26. Dilek, Y. Probing the Timing of the Onset of the Modern-Style Plate Tectonic Regime in Earth's History. *JGS* **2024**, *181*, jgs2024-122. [CrossRef]
27. Harrison, T.M. We Don't Know When Plate Tectonics Began. *JGS* **2024**, *181*, jgs2023-212. [CrossRef]
28. Dall'Agnol, R.; Oliveira, M.A.; Almeida, J.A.C.; Althoff, F.J.; Leite, A.A.S.; Oliveira, D.C.; Barros, C.E.M. Archean and Paleoproterozoic Granitoids of the Carajás Metallogenic Province, Eastern Amazonian Craton. In *Symposium on Magmatism, Crustal Evolution, and Metallogenesis of the Amazonian Craton*; Dall'Agnol, R., Rosa-Costa, L.T., Klein, E.L., Eds.; PRONEX/UFPA and SBG-NO: Belém, Brasil, 2006; p. 150.
29. Vasquez, M.L.; Rosa-Costa, L.T. *Geologia e Recursos Minerais do Estado do Pará: Sistema de Informações Geográficas – SIG: Texto Explicativo dos Mapas Geológico e Tectônico e de Recursos Minerais do Estado do Pará; Escala 1:1,000,000*; Serviço Geológico do Brasil (SGB): Belém, Brasil, 2008; p. 329.
30. Silva, R.C.S.; Sabóia, A.M.; Polo, H.J.O. *Projeto Integração Geológica-Geofísico -Metalogenética das Sequências de Greenstone Belts do Domínio Rio Maria - Novas Fronteiras Rio Maria, Escalas1:250,000 e 1:100,000 Estado do Pará*; Serviço Geológico do Brasil (SGB): Belém, Brasil, 2021; p. 269.
31. Leite, A.A.S.; Dall'Agnol, R.; Macambira, M.J.B.; Althoff, F.J. Geologia e Geocronologia Dos Granitóides Arqueanos Da Região de Xinguara-PA e Suas Implicações Na Evolução Do Terreno Granito-Greenstone de Rio Maria, Cráton Amazônico. *RBG* **2004**, *34*, 447–458. [CrossRef]
32. Almeida, J.A.C.; Dall'Agnol, R.; Oliveira, M.A.; Macambira, M.J.B.; Pimentel, M.M.; Rämö, O.T.; Guimarães, F.V.G.; Leite, A.A.S. Zircon Geochronology, Geochemistry and Origin of the TTG Suites of the Rio Maria Granite-Greenstone Terrane: Implications for the Growth of the Archean Crust of the Carajás Province, Brazil. *Precambrian Res.* **2011**, *187*, 201–221. [CrossRef]
33. Rolando, A.P.; Macambira, M.J.B. Archean Crust Formation in Inajá Range Area, SSE of Amazonian Craton, Brazil, Based on Zircon Ages and Nd Isotopes. In *South American Symposium on Isotope Geology*; Expanded Abstracts; SBG: Salvador, Brasil, 2003.
34. Costa, I.S.L.; Rocha, M.P.; Klein, E.L.; Vasquez, M.L. Lithospheric Structure of the Southern Amazonian Craton from Multiple-Frequency Seismic Tomography: Preliminary Insights on Tectonic and Metallogenic Implications. *J. S. Am. Earth Sci.* **2020**, *101*, 102608. [CrossRef]
35. Feio, G.R.L.; Dall'Agnol, R.; Dantas, E.L.; Macambira, M.J.B.; Santos, J.O.S.; Althoff, F.J.; Soares, J.E.B. Archean Granitoid Magmatism in the Canaã Dos Carajás Area: Implications for Crustal Evolution of the Carajás Province, Amazonian Craton, Brazil. *Precambrian Res.* **2013**, *227*, 157–185. [CrossRef]
36. Martins, P.L.G.; Toledo, C.L.B.; Silva, A.M.; Chemale, F., Jr.; Santos, J.O.S.; Assis, L.M. Neoarchean Magmatism in the Southeastern Amazonian Craton, Brazil: Petrography, Geochemistry and Tectonic Significance of Basalts from the Carajás Basin. *Precambrian Res.* **2017**, *302*, 340–357. [CrossRef]
37. Teixeira, M.F.B.; Dall'Agnol, R.; Santos, J.O.S.; Kemp, A.; Evans, N. Petrogenesis of the Paleoproterozoic (Orosirian) A-Type Granites of Carajás Province, Amazon Craton, Brazil: Combined in Situ Hf O Isotopes of Zircon. *Lithos* **2019**, *332–333*, 1–22. [CrossRef]
38. Marangoanha, B.; Oliveira, D.C.; Galarza, M.A.; Marques, G.T. Crustal Anatexis and Mantle-Derived Magmas Forming Neoarchean A-Type Granitoids in Carajás Province, Northern Brazil: Petrological Evidence and Tectonic Control. *Precambrian Res.* **2020**, *338*, 105585. [CrossRef]

39. Nascimento, A.C.; Oliveira, D.C.; Heilimo, E.; Galarza, M.A.; Gabriel, E.O.; Whitehouse, M.; Kurhila, M.; Lamarão, C.N. Crustal Contamination and Insights into Diachronous Changes toward Modern Tectonics: Evidence from Hf-Nd-O-Pb Isotope of Sanukitoids from the Amazonian Craton. *Geosci. Front.* **2025**, *16*, 102172. [CrossRef]
40. Silva, F.F.; Oliveira, D.C.; Dall'Agnol, R.; Santos, J.O.S.; Galarza, M.A.; Guimarães, F.V.; Sousa, L.A.M. Petrogenesis and Tectonic Settings of the Neoarchean A-Type Granitoid Complex from the Carajás Province, Amazonian Craton: Constraints from Geochemistry, SHRIMP U-Pb Zircon Geochronology and Hf–Nd Isotopes. *JGS* **2025**, *182*, jgs2024-109. [CrossRef]
41. Tassinari, C.C.G.; Macambira, M.J.B. Evolução Tectônica Do Cráton Amazônico. In *Geologia do continente Sul Americano. Evolução da obra de Almeida F.F.M.*; Mantesso Neto, V., Bartorelli, A., Carneiro, C.D.R., Brito Neves, B.B., Eds.; BECA: São Paulo, Brasil, 2004; pp. 471–486.
42. Rämö, O.T.; Dall'Agnol, R.; Macambira, M.J.B.; Leite, A.A.S.; Oliveira, D.C. 1.88 Ga Oxidized A-Type Granites of the Rio Maria Region, Eastern Amazonian Craton, Brazil: Positively Anorogenic! *J. Geol.* **2002**, *110*, 603–610. [CrossRef]
43. Santos, M.N.S.; Oliveira, D.C. Rio Maria Granodiorite and Associated Rocks of Ourilândia Do Norte – Carajás Province: Petrography, Geochemistry and Implications for Sanukitoid Petrogenesis. *J. S. Am. Earth Sci.* **2016**, *72*, 279–301. [CrossRef]
44. Silva, L.R.; Oliveira, D.C.; Nascimento, A.C.; Lamarão, C.N.; Almeida, J.A.C. The Mesoarchean Plutonic Complex from the Carajás Province, Amazonian Craton: Petrogenesis, Zircon U Pb SHRIMP Geochronology and Tectonic Implications. *Lithos* **2022**, *432–433*, 106901. [CrossRef]
45. Silva, L.R.; Oliveira, D.C.; Galarza, M.A.; Nascimento, A.C.; Marangoanha, B.; Marques, G.T. Zircon U–Pb–Hf Isotope and Geochemical Constraints on the Petrogenesis and Tectonic Setting of Mesoarchean Granitoids from the Carajás Province, Amazonian Craton, Brazil. *Precambrian Res.* **2023**, *398*, 107204. [CrossRef]
46. Teixeira, M.F.B.; Dall'Agnol, R.; Santos, J.O.S.; Oliveira, D.C.; Lamarão, C.N.; McNaughton, N.J. Crystallization Ages of Paleoproterozoic A-Type Granites of Carajás Province, Amazon Craton: Constraints from U-Pb Geochronology of Zircon and Titanite. *J. S. Am. Earth Sci.* **2018**, *88*, 312–331. [CrossRef]
47. Marangoanha, B.; Oliveira, D.C.; Dall'Agnol, R. The Archean Granulite-Enderbite Complex of the Northern Carajás Province, Amazonian Craton (Brazil): Origin and Implications for Crustal Growth and Cratonization. *Lithos* **2019**, *350–351*, 105275. [CrossRef]
48. Santos, R.F.S.; Oliveira, D.C.D.; Marangoanha, B.; Galarza, M.A.; Santos, M.R. Geochemistry, Zircon U-Pb Geochronology and Lu-Hf Isotopes of the Manda Saia Granite: Petrological Affinity and Magma Source of Evolved A-Type Granites from the Carajás Province, Southeastern Amazonian Craton, Brazil. *Lithos* **2023**, *462–463*, 107412. [CrossRef]
49. Zeh, A.; Cabral, A.R. Combining Detrital Zircon Shape and U–Pb–Hf Isotope Analyses for Provenance Studies – An Example from the Aquiri Region, Amazon Craton, Brazil. *Precambrian Res.* **2021**, *364*, 106343. [CrossRef]
50. Motta, J.G.; Souza Filho, C.R.D.; Carranza, E.J.M.; Braitenberg, C. Archean Crust and Metallogenic Zones in the Amazonian Craton Sensed by Satellite Gravity Data. *Sci. Rep.* **2019**, *9*, 2565. [CrossRef] [PubMed]
51. Azevedo, T.R.; Rodrigues, A.S.B.; Rolando, A.P.; Macambira, M.J.B. Estudo de Zircão Arqueano Na Resolução de Problemas Estratigráficos Da Região Da Serra Do Inajá, SE Do Cráton Amazônico. In *XLII Congresso Brasileiro de Geologia*; SBG: Araxá, Brasil, 2004; Volume 1 CD-ROM.
52. Villas, R.N.; de Lima, A.D.; Kotschoubey, B.; Neves, M.P.; Osborne, G.A. Contexto geológico e origem da mineralização sulfetada estratiforme de São Martim, SW do Cinturão Araguaia, Pará. *Rev. Bras. Geociências* **2007**, *37*, 305–323. [CrossRef]
53. Rocha, M.L.B.P.; Barros, M.A.D.S.; Lima, E.F.D.; Pierosan, R. Paleoproterozoic Domo of Lava from Iriri Group – Sonho Meu Farm – Northeast of Mato Grosso, Amazon Craton: Geology, Geochemistry, and Geochronology. *RBG* **2012**, *42*, 471–488. [CrossRef]
54. Roverato, M.; Giordano, D.; Giovanardi, T.; Juliani, C.; Polo, L. *The 2.0–1.88 Ga Paleoproterozoic Evolution of the Southern Amazonian Craton (Brazil): An Interpretation Inferred by Lithofaciological, Geochemical and Geochronological Data*; Gondwana Research 2019; Elsevier: Amsterdam, The Netherlands, 2019; pp. 1–24.
55. Vasquez, M.L.; Macambira, E.M.B.; Lafon, J.M.; Galarza, M.A. Datação Por Evaporação de Pb Em Zircão de Ortognaisses e Granitoides Da Região de Santana Do Araguaia-Sudeste Do Pará. In *Simpósio de Geologia da Amazônia*; Resumo Expandido; SBG–Núcleo Norte: Porto Velho, Brasil, 2007.
56. Monteiro, P.M.; Rolando, A.P.; Macambira, M.J.B. Proveniência de Zircão de Quartzitos Da Formação Gorotire e Grupo Rio Fresco, Serra Do Inajá, Sul Da Província Mineral Do Carajás. In *42° Congresso Brasileiro de Geologia*; Resumos, 1 CD-Rom; SBG: Araxá, Brasil, 2004.
57. Ribeiro, P.S.E.; Alves, C.L. *Geologia e Recursos Minerais da Região de Palmas-Folhas Miracema do Norte SC. 22- XD, Porto Nacional SC. 22-ZB e Santa Teresinha SC. 22-ZA: Estado do Tocantins*; Serviço Geológico do Brasil (SGB): Goiânia, BRasil, 2017.
58. Almeida, F.F.M.; Hasui, Y.; Brito Neves, B.B.; Fuck, R.A. Brazilian Structural Provinces: An Introduction. *Earth-Sci. Rev.* **1981**, *17*, 1–29. [CrossRef]
59. Dall'Agnol, R.; Teixeira, N.P.; Rämö, O.T.; Moura, C.A.V.; Macambira, M.J.B.; De Oliveira, D.C. Petrogenesis of the Paleoproterozoic Rapakivi A-Type Granites of the Archean Carajás Metallogenic Province, Brazil. *Lithos* **2005**, *80*, 101–129. [CrossRef]

60. Althoff, F.; Barbey, P.; Boullier, A.-M. 2.8–3.0 Ga Plutonism and Deformation in the SE Amazonian Craton: The Archaean Granitoids of Marajoara (Carajás Mineral Province, Brazil). *Precambrian Res.* **2000**, *104*, 187–206. [CrossRef]
61. Souza, Z.S.; Potrel, A.; Lafon, J.-M.; Althoff, F.J.; Martins Pimentel, M.; Dall'Agnol, R.; Oliveira, C.G. Nd, Pb and Sr Isotopes in the Identidade Belt, an Archaean Greenstone Belt of the Rio Maria Region (Carajás Province, Brazil): Implications for the Archaean Geodynamic Evolution of the Amazonian Craton. *Precambrian Res.* **2001**, *109*, 293–315. [CrossRef]
62. Oliveira, D.C.; Dall'Agnol, R.; Barros, C.E.M.; Oliveira, M.A. Geology, Geochemistry and Magmatic Evolution of the Paleoproterozoic, Anorogenic Oxidized A-Type Redenção Granite of the Jamon Suite, Eastern Amazonian Craton, Brazil. *Can. Mineral.* **2009**, *47*, 1441–1468. [CrossRef]
63. Almeida, J.A.C.; Dall'Agnol, R.; Leite, A.A.D.S. Geochemistry and Zircon Geochronology of the Archean Granite Suites of the Rio Maria Granite-Greenstone Terrane, Carajás Province, Brazil. *J. S. Am. Earth Sci.* **2013**, *42*, 103–126. [CrossRef]
64. Almeida, J.A.C.; Oliveira, V.E.S.D.; Rocha, J.L.S.; Feio, G.R.D.L.; Rocha, M.C.; Rocha, K.P.P.D. Caracterização Geológica, Geoquímica e Aerogeofísica Dos Granitoides Arqueanos Da Porção Sul Do Domínio Rio Maria. *Geol. USP Sér. Cient.* **2020**, *20*, 61–85. [CrossRef]
65. de Oliveira, R.G.; Domingos, N.R.R.; Medeiros, W.E. Deep Crustal Structure of the Sergipano Belt, NE-Brazil, Revealed by Integrated Modeling of Gravity, Magnetic, and Geological Data. *J. Geol. Surv. Braz.* **2023**, *6*, 1–22. [CrossRef]
66. Lafon, J.M.; Scheller, T. Geocronologia Pb/Pb Em Zircão Do Granodiorito Cumaru, Serra Dos Gradaús, PA. In *4° Simpósio de Geologia da Amazônia*; Resumos expandidos; SBG–Núcleo Norte: Belém, Brasil, 1994; pp. 321–323.
67. Guimarães, F.V.; Dall'Agnol, R.; Almeida, J.A.C.; Oliveira, M.A.D. Caracterização Geológica, Petrográfica e Geoquímica Do Trondhjemito Mogno e Tonalito Mariazinha, Terreno Granito-Greenstone Mesoarqueano de Rio Maria, SE Do Pará. *RBG* **2010**, *40*, 196–211. [CrossRef]
68. Souza, D.B. *Geologia e Petrologia dos Granitoides Arqueanos da Área de Tucumã: Implicações Para a Evolução Crustal da Província Carajás*; Exame de qualificação; Instituto de Geociências, Universidade Federal do Pará: Belém, Brasil, 2018.
69. Leite-Santos, P.J. Petrologia e Geocronologia das Associações Leucograníticas Arqueanas da Região de Água Azul do Norte (PA): Implicações Para a Evolução Crustal da Província Carajás. Ph.D. Thesis, Instituto de Geociências, PPGG, Universidade Federal do Pará, Belém, Brasil, 2016.
70. Tassinari, C.C.G.; Tachibana, J.; Tulio, M.; Livio, R.; Gaia, C. Geologia Isotópica Aplicada Nas Mineralizações de Cu-Au Do Greenstone Belt Da Serra Dos Gradaús, Província Mineral de Carajás, Cráton Amazônico: Exemplo de Mineralizações Policíclicas. In *Simpósio Brasileiro de Metalogenia*; Resumos; SBG,1 CD-ROM: Porto Alegre, Brasil, 2005.
71. Macambira, M.J.B.; Lancelot, J. Em Busca Do Embasamento Arqueano Da Região de Rio Maria, Sudeste Do Estado Do Pará. In *3° Simpósio de Geologia da Amazônia*; Resumos Expandidos; SBG: Porto Alegre, Brasil, 1991; pp. 49–58.
72. Macambira, M.J.B. Chronologie U-Pb, Rb-Sr, K-Ar et Croissance de La Croûte Continentale Dans l'Amazonie Du Sud-Est; Example de La Région de Rio Maria, Province de Carajás, Bresil. Ph.D. Thesis, Sciences et Techiniques du Langdoc, Universite Montpellier II, Montpellier, France, 1992.
73. Macambira, M.J.B.; Lafon, J.M.; Pidgeon, R.T. Crescimento Crustal Arqueano Registrado Em Zircões de Sedimentos Da Região de Rio Maria, Província Carajás, Pará. In *40° Congresso Brasileiro Geologia*; Anais: Belo Horizonte, Brasil; SBG: Porto Alegre, Brasil, 1998; Volume Anais, p. 55.
74. Barbosa, A.A.; Lafon, J.M.; Neves, A.P.; Vale, A.G. *Geocronologia Rb-Sr e Pb-Pb do Granito Redenção, SE do Pará: Implicações para a evolução do magmatismo proterozóico da região de Redenção*; Boletim do Museu Paraense Emílio Goeldi: Belém, Brasil, 1995; Volume 7, pp. 147–164.
75. Feio, G.R.L.; Dall'Agnol, R. Geochemistry and Petrogenesis of the Mesoarchean Granites from the Canaã Dos Carajás Area, Carajás Province, Brazil: Implications for the Origin of Archean Granites. *Lithos* **2012**, *154*, 33–52. [CrossRef]
76. Feio, G.R.L.; Dall'Agnol, R.; Dantas, E.L.; Macambira, M.J.B.; Gomes, A.C.B.; Sardinha, A.S.; Oliveira, D.C.; Santos, R.D.; Santos, P.A. Geochemistry, Geochronology, and Origin of the Neoarchean Planalto Granite Suite, Carajás, Amazonian Craton: A-Type or Hydrated Charnockitic Granites? *Lithos* **2012**, *151*, 57–73. [CrossRef]
77. Dall'Agnol, R.; Souza, Z.S.; Althoff, F.J.; Barros, C.E.M.; Leite, A.A.S.; Jorge João, X.S. General Aspects of the Granitogenesis of the Carajás Metallogenic Province. In *International Symposium on Granites and Associated Mineralizations; Extended Abstracts*; PRONEX/UFPA and SBG-NO: Salvador, Brasil, 1997; pp. 135–161.
78. Abrantes, F.R., Jr.; Lamarão, C.N. Petrografia e Variação Composicional de Zircão Do Granito Gradaús, Província Carajás, Centro-Sul Do Pará. In *Anais do 13° Congresso Brasileiro de Geoquímica & 3° Simpósio de Geoquímica dos Países do Mercosul, Gramado*; SBGq: Gramado, Brasil, 2011; Volume 2, pp. 713–716.
79. Machado, N.; Lindenmayer, Z.; Krogh, T.E.; Lindenmayer, D. U-Pb Geochronology of Archean Magmatism and Basement Reactivation in the Carajás Area, Amazon Shield, Brazil. *Precambrian Res.* **1991**, *49*, 329–354. [CrossRef]
80. Antonio, P.Y.J.; D'Agrella-Filho, M.S.; Trindade, R.I.F.; Nédélec, A.; De Oliveira, D.C.; Da Silva, F.F.; Roverato, M.; Lana, C. Turmoil before the Boring Billion: Paleomagnetism of the 1880–1860 Ma Uatumã Event in the Amazonian Craton. *Gondwana Res.* **2017**, *49*, 106–129. [CrossRef]

81. Rodrigues, E.M.S.; Lafon, J.M.; Scheller, T. Geocronologia Pb-Pb Em Rochas Totais Da Província Mineral de Carajás: Primeiros Resultados. In *37° Congresso Brasileiro de Geologia*; Resumos; SBG: São Paulo, Brasil, 1992; Volume 2, pp. 183–184.
82. Santos, R.F.S.; Oliveira, D.C.D.; Almeida, J.D.A.C.D.; Dall'Agnol, R.; Marangoanha, B.; Galarza, M.A.; Lamarão, C.N.; Silva, F.F.D. Petrogenesis and Emplacement of the Paleoproterozoic A-Type Marajoara Granite in the Carajás Province, Southeastern Amazonian Craton: Constraints from Geochemistry, Zircon Geochronology, Nd Hf Isotopes, Coexistence of Reduced and Oxidized Magmas and New Insights from a Composite Dike. *Lithos* **2025**, *514–515*, 108174. [CrossRef]
83. Althoff, F.J.; Macambira, M.J.B.; Scheller, T.; Dall'Agnol, R.; Lafon, J.M. La Croissance Du Craton Sud-Amazonien (Région de Rio Maria, Brésil). In *Réunion des Sciences de la Terre*; Societé Géologique de France: Brest, France, 1998; p. 62.
84. Pimentel, M.M.; Machado, N. Geocronologia U-Pb Do Terrenos Granito-Greenstone de Rio Maria, Pará. In *38° Congresso Brasileiro de Geologia*; Resumos expandidos; SBG: Camboriú, Brasil, 1994; pp. 390–391.
85. Macambira, M.J.B.; Lancelot, J. Time constraints for the formation of the Archean Rio Maria crust, southeastern Amazonian Craton, Brazil . *Int. Geol. Rev.* **1996**, *38*, 1134–1142. [CrossRef]
86. Lima, P.H.A. *Geologia, Petrografia e Geocronologia Do Granito São João, Província Carajás, SSE Do Pará. Trabalho de Conclusão de Curso, Faculdade de Geologia, Instituto de Geociências*; Universidade Federal do Pará: Belém, Brasil, 2011.
87. Milhomem Neto, J.M.; Lafon, J.M. Zircon U-Pb and Lu-Hf Isotope Constraints on Archean Crustal Evolution in Southeastern Guyana Shield. *Geosci. Front.* **2019**, *10*, 1477–1506. [CrossRef]
88. Gioia, S.M.C.L.; Pimentel, M.M. The Sm-Nd Isotopic Method in the Geochronology Laboratory of the University of Brasília. *An. Acad. Bras. Ciênc.* **2000**, *72*, 219–245. [CrossRef]
89. Fisher, C.M.; Vervoort, J.D. Using the Magmatic Record to Constrain the Growth of Continental Crust—The Eoarchean Zircon Hf Record of Greenland. *Earth Planet. Sci. Lett.* **2018**, *488*, 79–91. [CrossRef]
90. Shand, S.J. *The Eruptive Rocks*; John Wiley: New York, NY, USA, 1943.
91. Leite, A.A.S. Geoquímica, Petrogênese e Evolução Estrutural Dos Granitoides Arqueanos Da Região de Xinguara, SE Do Cráton Amazônico. PhD Tese, Instituto de Geociências, Programa de Pós-Graduação em Geologia e Geoquímica, Universidade Federal do Pará, Belém, Brasil, 2001.
92. Almeida, J.D.A.C.; Oliveira, M.A.; Moura, C.A.V.; Oliveira, D.C.; Althoff, F.J.; Costi, H.T.; Borges, R.M.K.; Dall'Agnol, R. *Geologia da folha Marajoara SB.22-Z-C-V; Programa Levantamentos Geológicos Básicos do Brasil—PLGB*; Serviço Geológico do Brasil (SGB): Brasília, Brazil, 2008; p. 147.
93. Dall'agnol, R.; Scaillet, B.; Pichavant, M. An Experimental Study of a Lower Proterozoic A-Type Granite from the Eastern Amazonian Craton, Brazil. *J. Petrol.* **1999**, *40*, 1673–1698. [CrossRef]
94. Santos, R.F. Origem e Construção dos Granitos Marajoara e Manda Saia: Contribuições Para a Definição da Natureza do Magmatismo Paleoproterozoico da Província Carajás. Ph.D. Thesis, Universidade Federal do Pará, Belém, Brasil, 2024.
95. Santos, R.F.S.; Oliveira, D.C.D.; Silva, F.F.D. Geocronologia U-Pb, Classificação e Aspectos Evolutivos Do Granito Marajoara, Província Carajás. *Geol. USP Sér. cient.* **2018**, *18*, 89–124. [CrossRef]
96. Silva, F.F.D.; Oliveira, D.C.D.; Antonio, P.Y.J.; D'Agrella Filho, M.S.; Lamarão, C.N. Bimodal Magmatism of the Tucumã Area, Carajás Province: U-Pb Geochronology, Classification and Processes. *J. S. Am. Earth Sci.* **2016**, *72*, 95–114. [CrossRef]
97. Avelar, V.G. Geocronologia Pb-Pb Por Evaporação em Monocristal de Zircão do Magmatismo da Região de Tucumã, SE do Estado do Pará, Amazônia Oriental. Ph.D. Dissertação, Instituto de Geociências, Universidade Federal do Pará, Belém, Brasil, 1996.
98. Paiva-Junior, A.L. Geologia, Petrografia, Geocronologia e Geoquímica Do Granito Anorogênico Seringa, Província Mineral de Carajás, SSE Do Pará. Ph.D. Dissertação, Instituto de Geociências, Universidade Federal do Pará, Belém, Brasil, 2009.
99. Andersen, T.; Andersson, U.B.; Graham, S.; Åberg, G.; Simonsen, S.L. Granitic Magmatism by Melting of Juvenile Continental Crust: New Constraints on the Source of Palaeoproterozoic Granitoids in Fennoscandia from Hf Isotopes in Zircon. *J. Geol. Soc.* **2009**, *166*, 233–247. [CrossRef]
100. Streckeisen, A. To Each Plutonic Rock Its Proper Name. *Earth-Sci. Rev.* **1976**, *12*, 1–33. [CrossRef]
101. Gibson, S.; Le Maitre, R.W. (Eds.) Igneous Rocks. A Classification and Glossary of Terms. Recommendations of the International Union of Geological Sciences Subcommission on the Systematics of Igneous Rocks. *Geol. Mag.* **2003**, *140*, 367. [CrossRef]
102. Warr, L.N. IMA–CNMNC Approved Mineral Symbols. *Mineral. Mag.* **2021**, *85*, 291–320. [CrossRef]
103. Debon, F.; le Fort, P. A Chemical–Mineralogical Classification of Common Plutonic Rocks and Associations. *Earth Environ. Sci. Trans. R. Soc. Edinb.* **1983**, *73*, 135–149. [CrossRef]
104. O'Connor, J.T. A Classification for Quartz-Rich Igneous Rocks Based on Feldspar Ratios. *US Geol. Surv. Prof. Pap.* **1965**, *525*, 79–84.
105. Barker, F. Trondhjemite: Definition, Environment and Hypotheses of Origin. In *Developments in Petrology*; Elsevier: Amsterdam, The Netherlands, 1979; Volume 6, pp. 1–12. ISBN 978-0-444-41765-7.
106. Frost, B.R.; Barnes, C.G.; Collins, W.J.; Arculus, R.J.; Ellis, D.J.; Frost, C.D. A Geochemical Classification for Granitic Rocks. *J. Petrol.* **2001**, *42*, 2033–2048. [CrossRef]
107. Irvine, T.N.; Baragar, W.R.A. A Guide to the Chemical Classification of the Common Volcanic Rocks. *Can. J. Earth Sci.* **1971**, *8*, 523–548. [CrossRef]

108. Peccerillo, A.; Taylor, S.R. Geochemistry of Eocene Calc-Alkaline Volcanic Rocks from the Kastamonu Area, Northern Turkey. *Contrib. Mineral. Petrol.* **1976**, *58*, 63–81. [CrossRef]
109. McDonough, W.F.; Sun, S.S. The Composition of the Earth. *Chem. Geol.* **1995**, *120*, 223–253. [CrossRef]
110. Boynton, W.V. Cosmochemistry of the Rare Earth Elements: Meteorite Studies. In *Developments in Geochemistry*; Elsevier: Amsterdam, The Netherlands, 1984; Volume 2, pp. 63–114. ISBN 978-0-444-42148-7.
111. Spencer, C.J.; Kirkland, C.L.; Taylor, R.J.M. Strategies towards Statistically Robust Interpretations of in Situ U-Pb Zircon Geochronology. *Geosci. Front.* **2016**, *7*, 581–589. [CrossRef]
112. Spencer, C.J.; Kirkland, C.L.; Roberts, N.M.W.; Evans, N.J.; Liebmann, J. Strategies towards Robust Interpretations of in Situ Zircon Lu–Hf Isotope Analyses. *Geosci. Front.* **2020**, *11*, 843–853. [CrossRef]
113. Fisher, C.M.; Vervoort, J.D.; Hanchar, J.M. Guidelines for Reporting Zircon Hf Isotopic Data by LA-MC-ICPMS and Potential Pitfalls in the Interpretation of These Data. *Chem. Geol.* **2014**, *363*, 125–133. [CrossRef]
114. Griffin, W.L.; Wang, X.; Jackson, S.E.; Pearson, N.J.; O'Reilly, S.Y.; Xu, X.; Zhou, X. Zircon Chemistry and Magma Mixing, SE China: In-Situ Analysis of Hf Isotopes, Tonglu and Pingtan Igneous Complexes. *Lithos* **2002**, *61*, 237–269. [CrossRef]
115. Griffin, W.L.; Belousova, E.A.; Shee, S.R.; Pearson, N.J.; O'Reilly, S.Y. Archean Crustal Evolution in the Northern Yilgarn Craton: U–Pb and Hf-Isotope Evidence from Detrital Zircons. *Precambrian Res.* **2004**, *131*, 231–282. [CrossRef]
116. Silva, M.A.D.; Monteiro, L.V.S.; Santos, T.J.S.; Moreto, C.P.N.; Sousa, S.D.; Faustinoni, J.M.; Melo, G.H.C.; Xavier, R.P.; Toledo, B.A.M. Mesoarchean Migmatites of the Carajás Province: From Intra-Arc Melting to Collision. *Lithos* **2021**, *388–389*, 106078. [CrossRef]
117. Othman, D.B.; Polvé, M.; Allègre, C.J. Nd-Sr Isotopic Composition of Granulites and Constraints on the Evolution of the Lower Continental Crust. *Nature* **1984**, *307*, 510–515. [CrossRef]
118. DePaolo, D.J. *Neodymium Isotope Geochemistry: An Introduction*; Springer: Berlin, Germany, 1988.
119. Trunfull, E.F.; Hagemann, S.G.; Xavier, R.P.; Moreto, C.P. Critical assessment of geochronological data from the Carajás Mineral Province, Brazil: Implications for metallogeny and tectonic evolution. *Ore Geol. Rev.* **2020**, *121*, 103556. [CrossRef]
120. Reis, Y.H.D.C.; Oliveira, D.C.D.; Silva-Silva, L.C.; Felix, W.Q.; Marangoanha, B.; Galarza, M.A.; Almeida, J.D.A.C.D. TTG Petrogenesis and U–Pb SHRIMP Zircon Geochronology Constraints on the Tectonic Regime and Formation of the Mesoarchean Crust from the Ourilândia–Tucumã Area in the Carajás Province, Amazonian Craton, Brazil. *Precambrian Res.* **2025**, *422*, 107767. [CrossRef]
121. Almeida, J.A.C.; Dall'Agnol, R.; Dias, S.B.; Althoff, F.J. Origin of the Archean Leucogranodiorite–Granite Suites: Evidence from the Rio Maria Terrane and Implications for Granite Magmatism in the Archean. *Lithos* **2010**, *120*, 235–257. [CrossRef]
122. Lameyre, J.; Bowden, P. Plutonic Rock Types Series: Discrimination of Various Granitoid Series and Related Rocks. *J. Volcanol. Geotherm. Res.* **1982**, *14*, 169–186. [CrossRef]
123. Rapp, R.P.; Shimizu, N.; Norman, M.D.; Applegate, G.S. Reaction between Slab-Derived Melts and Peridotite in the Mantle Wedge: Experimental Constraints at 3.8 GPa. *Chem. Geol.* **1999**, *160*, 335–356. [CrossRef]
124. Defant, M.J.; Drummond, M.S. Derivation of Some Modern Arc Magmas by Melting of Young Subducted Lithosphere. *Nature* **1990**, *347*, 662–665. [CrossRef]
125. Halla, J.; Van Hunen, J.; Heilimo, E.; Hölttä, P. Geochemical and Numerical Constraints on Neoarchean Plate Tectonics. *Precambrian Res.* **2009**, *174*, 155–162. [CrossRef]
126. Moyen, J.-F. The Composite Archaean Grey Gneisses: Petrological Significance, and Evidence for a Non-Unique Tectonic Setting for Archaean Crustal Growth. *Lithos* **2011**, *123*, 21–36. [CrossRef]
127. Schiano, P.; Monzier, M.; Eissen, J.-P.; Martin, H.; Koga, K.T. Simple Mixing as the Major Control of the Evolution of Volcanic Suites in the Ecuadorian Andes. *Contrib. Mineral. Petrol.* **2010**, *160*, 297–312. [CrossRef]
128. Heilimo, E.; Halla, J.; Hölttä, P. Discrimination and Origin of the Sanukitoid Series: Geochemical Constraints from the Neoarchean Western Karelian Province (Finland). *Lithos* **2010**, *115*, 27–39. [CrossRef]
129. Martin, H. Petrogenesis of Archaean Trondhjemites, Tonalites, and Granodiorites from Eastern Finland: Major and Trace Element Geochemistry. *J. Petrol.* **1987**, *28*, 921–953. [CrossRef]
130. Almeida, J.D.A.C.; Dall'agnol, R.; Rocha, M.C. Tonalite–Trondhjemite and Leucogranodiorite–Granite Suites From the Rio Maria Domain, Carajás Province, Brazil: Implications For Discrimination and Origin of the Archean Na-Granitoids. *Can. Mineral.* **2017**, *55*, 437–456. [CrossRef]
131. Champion, D.C.; Smithies, R.H. Archaean Granites of the Yilgarn and Pilbara Cratons, Western Australia. *Geosci. Aust.* **2001**, *4*, 134–136.
132. Green, T.H.; Pearson, N.J. An Experimental Study of Nb and Ta Partitioning between Ti-Rich Minerals and Silicate Liquids at High Pressure and Temperature. *Geochim. Cosmochim. Acta* **1987**, *51*, 55–62. [CrossRef]
133. López, S.; Castro, A.; García-Casco, A. Production of Granodiorite Melt by Interaction between Hydrous Mafic Magma and Tonalitic Crust. Experimental Constraints and Implications for the Generation of Archaean TTG Complexes. *Lithos* **2005**, *79*, 229–250. [CrossRef]

134. Martin, H.; Smithies, R.H.; Rapp, R.; Moyen, J.-F.; Champion, D. An Overview of Adakite, Tonalite–Trondhjemite–Granodiorite (TTG), and Sanukitoid: Relationships and Some Implications for Crustal Evolution. *Lithos* **2005**, *79*, 1–24. [CrossRef]
135. Rapp, R.P.; Shimizu, N.; Norman, M.D. Growth of Early Continental Crust by Partial Melting of Eclogite. *Nature* **2003**, *425*, 605–609. [CrossRef]
136. Moyen, J.-F.; Stevens, G.; Kisters, A.F.M.; Belcher, R.W.; Lemirre, B. TTG Plutons of the Barberton Granitoid-Greenstone Terrain, South Africa. In *Earth's Oldest Rocks*; Elsevier: Amsterdam, The Netherlands, 2019; pp. 615–653.
137. Champion, D.C.; Smithies, R.H. Chapter 4.3 Geochemistry of Paleoarchean Granites of the East Pilbara Terrane, Pilbara Craton, Western Australia: Implications for Early Archean Crustal Growth. In *Developments in Precambrian Geology*; Elsevier: Amsterdam, The Netherlands, 2007; Volume 15, pp. 369–409. ISBN 978-0-444-52810-0.
138. Galarza, M.A.; Oliveira, D.C.; Rodrigues, E.A.; Santos, A.N.; Martins, A.C.; Marangoanha, B. Neoarchean Granitoids (2.73–2.74 Ga) Intrusive and Associated with the Pium Diopside- Norite, Canaã Dos Carajás, Carajás Province (PA). In *Contribuições à geologia da Amazônia*; Lima, A.M., Gorayeb, P., Eds.; SBG-Núcleo Norte: Belém, Brasil, 2017; Volume 10, pp. 225–246.
139. Santos, P.A.D.; Teixeira, M.F.B.; Dall'Agnol, R.; Guimarães, F.V. Geologia, Petrografia e Geoquímica Da Associação Tonalito-Trondhjemito-Granodiorito (TTG) Do Extremo Leste Do Subdomínio de Transição, Província Carajás, Pará. *Bcnaturais* **2013**, *8*, 257–290. [CrossRef]
140. Vervoort, J.D.; Kemp, A.I.S. Clarifying the Zircon Hf Isotope Record of Crust–Mantle Evolution. *Chem. Geol.* **2016**, *425*, 65–75. [CrossRef]
141. Kemp, A.I.S.; Vervoort, J.D.; Petersson, A.; Smithies, R.H.; Lu, Y. A Linked Evolution for Granite-Greenstone Terranes of the Pilbara Craton from Nd and Hf Isotopes, with Implications for Archean Continental Growth. *Earth Planet. Sci. Lett.* **2023**, *601*, 117895. [CrossRef]
142. Petersson, A.; Waight, T.; Kemp, A.I.S.; Whitehouse, M.J. Refining Hf Crust Formation Ages in Precambrian Terranes. *Geochem. Persp. Let.* **2024**, *32*, 7–13. [CrossRef]
143. Mulder, J.A.; Nebel, O.; Gardiner, N.J.; Cawood, P.A.; Wainwright, A.N.; Ivanic, T.J. Crustal Rejuvenation Stabilised Earth's First Cratons. *Nat. Commun.* **2021**, *12*, 3535. [CrossRef]
144. Jackson, S.E.; Pearson, N.J.; Griffin, W.L.; Belousova, E.A. The Application of Laser Ablation-Inductively Coupled Plasma-Mass Spectrometry to in Situ U–Pb Zircon Geochronology. *Chem. Geol.* **2004**, *211*, 47–69. [CrossRef]
145. Teixeira, N.P.; Moura, C.A.V.; Bettencourt, J.S. Evidência Da Existência de Crosta Arqueana de 3,68 Ga Obtida Em Zircão de Rocha Gnáissica Tonalítica Do Complexo Xingu, No Segmento Oeste Da Província Mineral de Carajás, Região de São Felix Do Xingu, Estado Do Pará, Brasil. In *7th Simpósio de Geologia da Amazônia*; Resumos expandidos, 1 CD-ROM; SBG-Núcleo Norte: Belém, Brasil, 2001.
146. Mackenzie, W.S.; Donaldson, C.H.; Guilford, C. *Atlas de Igneous Rocks and Their Textures*; Longman Group Ltd.: Harlow Essex, UK, 1982.
147. Hutchison, C.S. *Laboratory Handbook of Petrographic Techniques*; Wiley: New York, NY, USA, 1974; ISBN 978-0-471-42550-2.
148. Deer, W.A.; Howie, R.A.; Zussman, J. *Rock-Forming Minerals. 2,B: Double-Chain Silicates*; Longman: London, UK, 1997; ISBN 978-1-897799-77-2.
149. Le Maitre, R.W.; Streckeisen, A.; Zanettin, B.; Le Bas, M.J.; Bonin, B.; Bateman, P. (Eds.) *Igneous Rocks: A Classification and Glossary of Terms, Recommendations of the International Union of Geological Sciences Subcommission on the Systematics of Igneous Rocks*; Cambridge University Press: Cambridge, UK, 2002; ISBN 978-0-511-53558-1.
150. Vernon, R.H. *A Practical Guide to Rock Microstructure*, 1st ed.; Cambridge University Press: Cambridge, UK, 2004; ISBN 978-0-521-81443-0.
151. Winter, J.D. *Principles of Igneous and Metamorphic Petrology*, 2nd ed.; Pearson Education: London, UK, 2014; ISBN 978-1-292-02153-9.
152. Wiedenbeck, M.; Allé, P.; Corfu, F.; Griffin, W.L.; Meier, M.; Oberli, F.; Quadt, A.V.O.N.; Roddick, J.C.; Spiegel, W. Three Natural Zircon Standards for U-Th-Pb, Lu-Hf, Trace Element and REE Analyses. *Geostand. Newsl.* **1995**, *19*, 1–23. [CrossRef]
153. Black, L.P.; Gulson, B.L. The age of the mud tank carbonatite, strangways range, northern territory. *J. Aust. Geol. Geophys.* **1978**, *3*, 227–232.
154. Stacey, J.S.; Kramers, J.D. Approximation of Terrestrial Lead Isotope Evolution by a Two-Stage Model. *Earth Planet. Sci. Lett.* **1975**, *26*, 207–221. [CrossRef]
155. Chemale, F., Jr.; Kawashita, K.; Dussin, I.A.; Ávila, J.N.; Justino, D.; Bertotti, A.L. U-Pb Zircon in Situ Dating with LA-MC-ICP-MS Using a Mixed Detector Configuration. *An. Acad. Barsileira Ciênc.* **2012**, *84*, 275–295. [CrossRef]
156. Ludwig, K.R. Mathematical-Statistical Treatment of Data and Errors for 230Th/U Geochronology. *Rev. Mineral. Geochem.* **2003**, *52*, 631–656. [CrossRef]
157. Russell, W.A.; Papanastassiou, D.A.; Tombrello, T.A. Ca Isotope Fractionation on the Earth and Other Solar System Materials. *Geochim. Cosmochim. Acta* **1978**, *42*, 1075–1090. [CrossRef]
158. Thirlwall, M.F.; Anczkiewicz, R. Multidynamic Isotope Ratio Analysis Using MC–ICP–MS and the Causes of Secular Drift in Hf, Nd and Pb Isotope Ratios. *Int. J. Mass. Spectrom.* **2004**, *235*, 59–81. [CrossRef]

159. Patchett, P.J.; Tatsumoto, M. A Routine High-Precision Method for Lu-Hf Isotope Geochemistry and Chronology. *Contrib. Mineral. Petrol.* **1981**, *75*, 263–267. [CrossRef]
160. Chu, N.C.; Taylor, R.N.; Chavagnac, V.; Nesbitt, R.W.; Boella, R.M.; Milton, J.A.; German, C.R.; Bayon, G.; Burton, K. Hf Isotope Ratio Analysis Using Multi-Collector Inductively Coupled Plasma Mass Spectrometry: An Evaluation of Isobaric Interference Corrections. *J. Anal. At. Spectrom.* **2002**, *17*, 1567–1574. [CrossRef]
161. Woodhead, J.D.; Hergt, J.M. A Preliminary Appraisal of Seven Natural Zircon Reference Materials for in Situ Hf Isotope Determination. *Geostand. Geoanalytical Res.* **2005**, *29*, 183–195. [CrossRef]
162. Scherer, E.; Münker, C.; Mezger, K. Calibration of the Lutetium-Hafnium Clock. *Science* **2001**, *293*, 683–687. [CrossRef] [PubMed]
163. Söderlund, U.; Patchett, P.J.; Vervoort, J.D.; Isachsen, C.E. The 176Lu Decay Constant Determined by Lu–Hf and U–Pb Isotope Systematics of Precambrian Mafic Intrusions. *Earth Planet. Sci. Lett.* **2004**, *219*, 311–324. [CrossRef]
164. Bouvier, A.; Vervoort, J.D.; Patchett, P.J. The Lu–Hf and Sm–Nd Isotopic Composition of CHUR: Constraints from Unequilibrated Chondrites and Implications for the Bulk Composition of Terrestrial Planets. *Earth Planet. Sci. Lett.* **2008**, *273*, 48–57. [CrossRef]
165. DePaolo, D.J. Trace Element and Isotopic Effects of Combined Wallrock Assimilation and Fractional Crystallization. *Earth Planet. Sci. Lett.* **1981**, *53*, 189–202. [CrossRef]

https://doi.org/10.3390/min16050483